Research Paper

Experimental investigation and tomography analysis of Darcy-Forchheimer flows in thermal protection systems

Shaolin Liu [a,b,*], Azita Ahmadi-Senichault [a,b], Hermes Scandelli [a,b], Jean Lachaud [b,c]

[a] *Arts et Métiers Institute of Technology, 33400, Talence, France*
[b] *I2M - Institute of Mechanical Engineering of Bordeaux: UMR CNRS 5295, University of Bordeaux, Arts et Métiers Institute of Technology, Hesam Université, Bordeaux INP, INRAE, 33400, Talence, France*
[c] *Univ. Bordeaux, 33400, Talence, France*

ARTICLE INFO

ABSTRACT

In thermal protection systems (TPS), Darcy's law or Darcy-Forchheimer's law is employed to model the pyrolysis gas flow within the anisotropic porous ablator depending on the flow regime considered. A key challenge with using these laws is first, the knowledge of the validity domain of each flow regime in terms of a critical Reynolds number (Re_c). Secondly, the lack of data on macroscopic properties, namely, the permeability and Forchheimer tensors is particularly challenging for the relevance of the models. The objective of this work is to contribute to overcoming these challenges by performing experimental and X-ray tomographic image-based characterization of Calcarb, a commercial carbon preform used for manufacturing TPS. For this purpose, fluid flow within Calcarb was studied experimentally in the Through-Thickness (TT) and the In-Plane (IP) directions for Reynolds numbers of 0.05 to 10.46 -representative of the TPS application. Tomography image-based micro-scale simulations, involving the direct resolution of the Navier–Stokes equations under both flow regimes, were also performed. Experimental results exhibit the anisotropic nature of Calcarb, namely through Re_c values, corresponding to the Darcy flow regime limit, slightly different in the two directions (Re_c of 0.31 and 0.43) with measured permeability values of 1.248×10^{-10} m^2 and 1.615×10^{-10} m^2 for TT and IP directions respectively. In the Forchheimer regime, experimental Forchheimer coefficients β were 2.0010×10^5 m^{-1} (TT) and 1.4948×10^5 m^{-1} (IP). During the simulation process, a numerical strategy was defined to obtain the permeability tensor yielding values within 8% of the experimental ones. The comparison of experimental results vs simulation results in the Forchheimer regime was performed through the analysis of the pressure gradients as functions of Re in the x, y, and z directions. The numerical estimations were compared successfully with experimental measurements, with a discrepancy of 5.2%, for Re values up to 2.4.

1. Introduction

Thermal protection systems (TPS) are essential for maintaining acceptable temperatures on a spacecraft's outer surface during all mission phases, especially during atmospheric re-entry [1–3]. TPS materials can be classified into two main categories: ablative materials [4], used in the Apollo missions [5], Stardust (NASA, 2006) [2,6], Mars Science Laboratory (NASA, 2012) [7,8], and Mars 2020 (NASA, 2021) [9]; and non-ablative materials, such as the ceramic tiles used on the space shuttle [10]. Ablative materials can be further subdivided into charring (pyrolyzing) and non-charring ablators. Pyrolyzing ablators primarily consist of a resin that fills the pores of a carbon matrix [4,11,12], such as FiberForm produced by Fiber Materials Inc. [13] and Calcarb produced by Mersen. During the pyrolysis process, the polymer matrix undergoes carbonization, generating pyrolysis gases that are

transported out of the material through the pore network via diffusion and convection. Simulating pyrolysis gas flow within the TPS is crucial, as these gases can significantly impact re-entry modeling.

A steady-state momentum equation for calculating the gas velocity within an ablator has been proposed [11]:

$$\langle \mathbf{v_g} \rangle = -\frac{1}{\mu} \frac{1 + \beta_0/p}{1 + Fo} \mathbf{K} \cdot \nabla \langle p \rangle^g \tag{1}$$

where $\langle \mathbf{v_g} \rangle$ is the superficial average velocity, referred to as the filtration velocity or Darcy velocity [14], and where $\langle p \rangle^g$ is the intrinsic average pressure. The permeability, $\mathbf{K}$, is a second-order tensor since most materials are anisotropic. The Klinkenberg coefficient, β_0, accounts for a slip at the gas-solid interface at the pore scale and is significant when the Knudsen number is not small [13,15]. The Forchheimer number, Fo ($\beta K \rho |\langle v_g \rangle|/\mu$), accounts for the convective flux

---

and Fo leads to Darcy's law [16], where gas velocity varies linearly with the pressure gradient. Neglecting only β_0 results in Forchheimer's law [14,17], where gas velocity varies nonlinearly. Numerous studies have employed Darcy's law to examine pyrolysis gas behavior [2,8,12,18,19], as gas velocity remains below 50 m/s during the pyrolysis process [8]. However, Martin et al. [4] found that using Forchheimer's law, while not significantly affecting temperature distribution, could impact inner pressure variations, potentially causing spallation. A key challenge with using these laws is first, the knowledge of the validity domain of each flow regime in terms of a critical Reynolds number (Re_c). Secondly, the lack of data on macroscopic properties, namely, the permeability and Forchheimer tensors is particularly challenging for the relevance of the models. In previous work, [20], micro-scale simulations were performed to solve the Navier–Stokes equations under the Darcy flow assumption, and the permeability tensor was predicted based on the results. The permeability was then compared with values obtained by Borner et al. [21] using direct simulation Monte Carlo methods, revealing an error of nearly 42%. The objective of this work is to contribute to overcoming these challenges by performing experimental and X-ray tomographic image-based characterization of Calcarb, a commercial carbon preform used for manufacturing TPS.

To provide a detailed overview of the state-of-the-art, let us start by presenting Darcy's law and Forchheimer's law for anisotropic porous media. The tensorial form of both laws for the case of negligible gravity is given in Eq. (2) [22,23],

$$\begin{cases} \langle \mathbf{v_g} \rangle = -\dfrac{\mathbf{K}}{\mu} \cdot \nabla \langle p \rangle^g \\ \langle \mathbf{v_g} \rangle = -\dfrac{\mathbf{K}}{\mu} \cdot \nabla \langle p \rangle^g - \mathbf{F} \cdot \langle \mathbf{v_g} \rangle \end{cases} \quad (2)$$

where superficial and intrinsic phase averages of any quantity φ_i associated with the i-phase are given by $\langle \varphi_i \rangle = \frac{1}{V} \int_{V_i} \varphi_i dV$ and $\langle \varphi_i \rangle^i = \varepsilon_i^{-1} \langle \varphi_i \rangle = \frac{1}{V_i} \int_{V_i} \varphi_i dV$, respectively. In these relationships, V_i denotes the volume of the i-phase contained within the averaging volume V, which represents a representative elementary volume of the porous medium. For the pressure term, $\langle p \rangle^g = \frac{1}{V_g} \int_{V_g} p dV$, while for the velocity term, $\langle \mathbf{v_g} \rangle = \frac{1}{V} \int_{V_g} \mathbf{v_g} dV$. **F** is the Forchheimer correction tensor and the last term $\mathbf{F} \cdot \langle \mathbf{v_g} \rangle$ is called the Forchheimer term [24]. There is no assumption on the dependence of **F** on $\langle \mathbf{v_g} \rangle$ in this general formulation. In the work of Wang et al. [23], **F** has been expressed as follows: $\mathbf{F} = (\mathbf{K} \cdot \boldsymbol{\beta}) |\langle \mathbf{v_g} \rangle| \rho / \mu$, where **K** is the permeability tensor, $\boldsymbol{\beta}$ is the Forchheimer coefficient tensor. It should be noted that $\boldsymbol{\beta}$ in this expression is considered as an independent property dependent only on the geometry of the microstructure. Therefore the expression presents a linear dependence of **F** on the velocity magnitude, i.e. quadratic Forchheimer term. Other parameters are the gas viscosity μ and density ρ. Two main approaches can be utilized to estimate the permeability and Forchheimer correction tensors numerically: one based on direct micro-scale simulations using classical Navier–Stokes equations, and the other on upscaling theories and solving of the associated closure problems [14,17,20,24,25]. In cases involving periodic media or when dealing with representative elementary volumes, both methods provide the same results. However, defining a numerical approach for non-periodic anisotropic porous media still remains necessary. In the first method, the permeability tensor, as derived from Darcy's law, is determined by solving the Navier–Stokes equations to obtain pressure and velocity terms which are then suitably averaged [20,25]. In the second method, the permeability tensor and Forchheimer correction tensor can be numerically estimated by solving a closure problem on a periodic unit cell representative of the structure, such as arrays of spheres [14,17] or a digital structure based on tomographic images of porous media, such as porous rocks [24]. The permeability tensor **K** should be symmetric (and positive definite) and depends solely on the structure of the porous medium. The Forchheimer correction tensor **F** relies on various parameters, such as structure, Reynolds number, and pressure gradient direction [14].

and should be taken into account when gas velocities exceed 50 m/s (that is, in high-density ablative materials submitted to very high heat fluxes) [4,15]. Simplifying the momentum equation by neglecting β_0

Table 1
Empirical numerical correlations for the Forchheimer coefficient β.

Investigators	Media	Method	Correlation	Remarks
Martin et al. [4]	Carbon phenolic	Experimental	$K = \frac{d_p^2 \varepsilon_g^3}{150(1-\varepsilon_g)^2}$, $\beta = \frac{\beta_k}{\sqrt{K}} = \frac{1}{7}\frac{1}{\varepsilon_g^{3/2}}\frac{1}{\sqrt{K}}$, $Fo = \beta_k \frac{\sqrt{K}\rho|\langle v_g\rangle|}{\mu}$	Ergun's equation for a packed bed
Wang et al. [23]	Arrays of spheres	Experimental	$\boldsymbol{\beta} = 10^{-3.25}\mathbf{K}^{-1.023}\boldsymbol{\tau}^{1.943}$ $logC_{ii} = -3.25 + 2.006 \cdot log\tau_{ii}$ $\mathbf{C} = \mathbf{K} \cdot \boldsymbol{\beta}$	τ is tortuosity tensor, $\mathbf{C}$ is product tensor
Petrasch et al.[35]	Porous ceramic	Pore-scale numerical simulation	$K = \frac{d_p^2}{64\varepsilon_s^{3/2}(1+56\varepsilon_s^3)}$, $\beta = \frac{0.550}{\sqrt{K}}$	K used the classical correction for fibrous media
Ahn et al. [31,36,37]	Ceramic ablators	Experimental	$K = 9.78 \times 10^{-11}\varepsilon_g^{0.381}$ $\beta = 1.222(1/\sqrt{K})$	$K = 10^{-10} - 10^{-15}$ m^{-2}
Aguilar et al. [24]	Porous rocks	Pore-scale numerical simulation	Forchheimer term $\propto \langle v_g\rangle^n$ exponent n are around 1.74–4.18	

In terms of experiments, measurements of the Forchheimer coefficient β for TPS materials have not been reported in the literature. However, data is available for various other materials, such as porous carbon foams [26], porous ceramic foams [27], porous rocky materials [28], and carbon fiber electrode backing layers [29]. During the experimental process, the volumetric flow rate and pressure drop across the porous sample are typically measured. Subsequently, the permeability and Forchheimer coefficient can be obtained by fitting either Darcy's law or Forchheimer's law in one dimension to the experimental data. The concept of effective permeability K_{eff}, proposed by Sobieski et al. [30], is utilized to analyze the variation between different flow regimes. In Darcy's flow, effective permeability is equivalent to permeability, while in Forchheimer's flow, it represents the combined effect of permeability and the Forchheimer coefficient. Marschall et al. [31,32] proposed a method for measuring the permeability of porous refractory insulators at room temperature, with measurements performed for both in-plane and transverse sample orientations. This method has been applied to various materials, such as silica-based tiles, PICA, and ceramics. Panerai et al. [13] further extended the experimental conditions to measure the permeability of carbon fibers at high temperatures, up to 1503 K. These experiments [13,31,32] are focused on investigating the permeability in the slip regime, that is, considering the Klinkenberg effect.

Both experimental and numerical methods have been employed to derive numerous correlations for the Forchheimer coefficient β or tensor $\boldsymbol{\beta}$ in various porous materials. A summary of the most widely used correlations and their validity ranges can be found in Table 1. One of the simplest forms of the Forchheimer coefficient β is presented by Martin et al. [4], who used Ergun's equation [33]. It should be noted that Ergun's equation is commonly employed to describe gas flow through packed beds [34]. Aguilar et al. [24] utilized digital images of porous rocks as microstructures, while Lasseux et al. [14] employed simple unit 2D cells with ordered and disordered arrangement of solid squares. Both approaches applied the volume averaging method and closure problems for solving the permeability and the Forchheimer coefficient or tensor. Although the correlations in Table 1 can provide some straightforward reference values, further research through experiments and micro-scale simulations is necessary to accurately determine the permeability tensor and Forchheimer coefficient tensor.

The objective of this work is to identify the validity domain of each flow regime in terms of a critical Reynolds number (Re_c) and to determine macroscopic properties, namely, the permeability and Forchheimer tensors by performing experimental and X-ray tomographic image-based characterization of Calcarb. For this purpose, fluid flow within Calcarb is studied experimentally in the Through-Thickness (TT) and the In-Plane (IP) directions for Reynolds numbers of 0.05 to 10.46 -representative of the TPS application. The remainder of the article is organized into four sections. In Section 2, the experimental setup and the porous sample are presented. In Section 3, the numerical method employed for micro-scale simulation is described. In Section 4, the

experimental and numerical results of permeability and Forchheimer coefficients for TT and IP directions are presented and discussed, followed by a comparison of these two sets of results. Conclusions and outlook are discussed in Section 5.

2. Experimental method

This section presents the experimental setup, sample characteristics, and data analysis method. In the first subsection, a detailed description of the experimental procedures is provided, along with a discussion of the uncertainties associated with the experimental setup. The second subsection focuses on the structural properties of the Calcarb samples. Lastly, the third subsection outlines the process of analyzing the experimental data.

2.1. Experimental setup and test procedure

A schematic drawing and photograph of the experimental setup that we have developed to measure the pressure drop in Calcarb are displayed in Fig. 1. The setup consists of a gas inlet, a mass flow controller, a pressure transmitter, and a quartz cylindrical tube that contains the sample. The nature of the gas does not affect the permeability that is a geometrical property. Pure nitrogen gas is used in this work for a better control of gas properties, namely, viscosity and density. Nitrogen is steadily supplied through a piping system. The mass-flow rate is controlled and measured by the mass-flow controller (Bronkhorst) with a range of 0.05 to 10 L/min (q_v), that is, a mass flow rate of Nitrogen, q_m ranging from 9.6×10^{-7} kg/s to 1.92×10^{-4} kg/s at room temperature. The Darcy velocity $\langle v_g\rangle$ varies from 0.0105 m/s to 2.1 m/s. The mass-flow controller's accuracy is $\pm 0.5\%$ of the reading. The pressure drop is measured using a differential pressure transmitter (EMERSON FISHER ROSEMOUNT) with an uncertainty of $\pm 0.055\%$ F.S. (Full Span is 0–620 mbar). The inlet and outlet pressure measurement points are indicated by red dots in Fig. 1(a). The electrical signal detected by the transmitter is then relayed to a data acquisition system for display. The sample of a length of 20 mm and a diameter of 10 mm is positioned within the test section. To assess the anisotropic properties of the materials, experiments were conducted on samples oriented differently relative to the microstructure of the fibrous porous media (sample 1: Through-Thickness (TT) and sample 2: In-Plane (IP)).

In this study, all experiments were carried out in triplicate. For the lower nitrogen flow range (0.05 to 3 L/min), pressure differences were measured at 20 distinct flow rate levels, while for the higher nitrogen flow range (3 L/min to 10 L/min), pressure differences were measured at 30 distinct flow rate levels. The ambient temperature was recorded for each test, with a value of 20 ± 1 °C.

(a) experimental setup
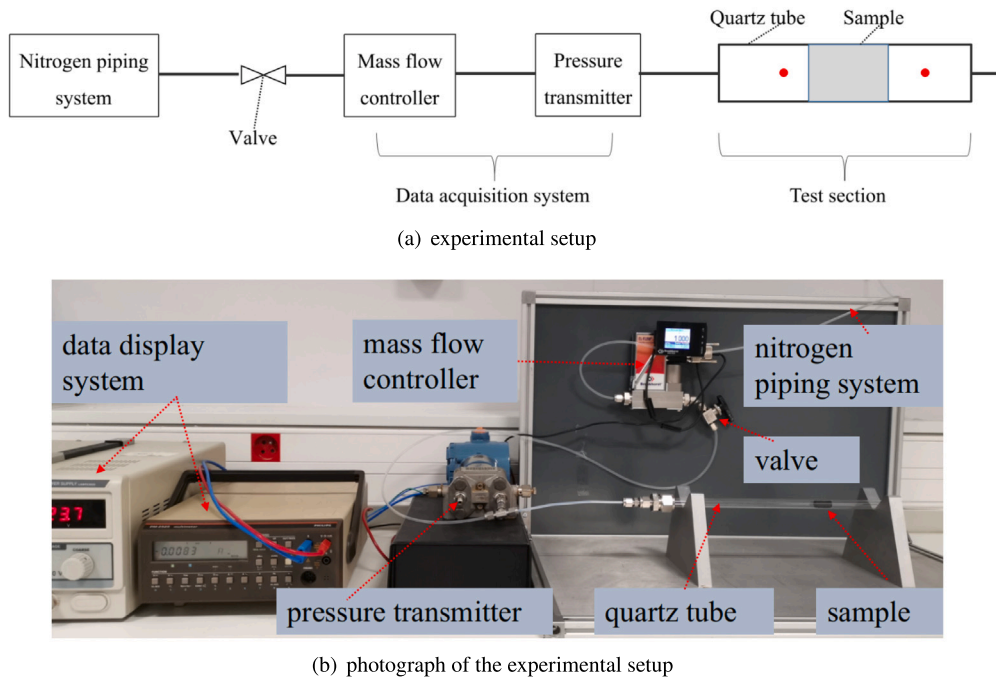

(b) photograph of the experimental setup

Fig. 1. Schematic diagram and photograph of the experimental system. (For interpretation of the references to color in this figure legend, the reader is referred to the web version of this article.)
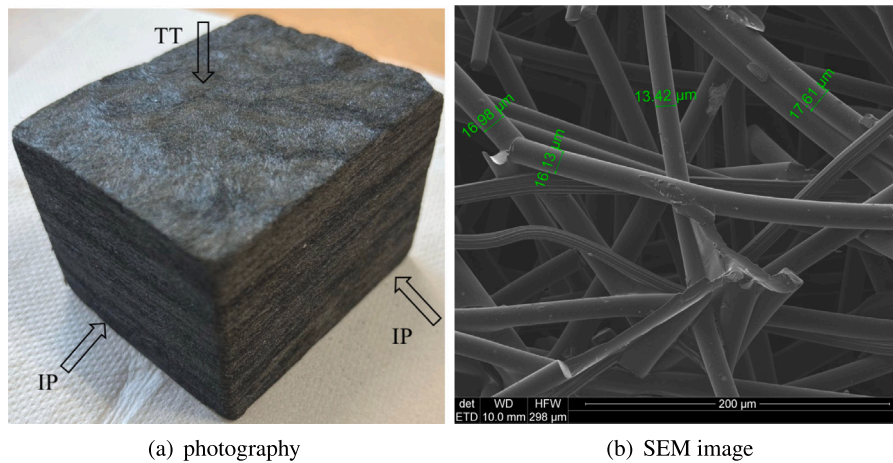

(a) photography

(b) SEM image

Fig. 2. Macro and micro-scale structures of Calcarb.

2.2. Description of Calcarb

Calcarb is composed of chopped carbon fibers with 1 millimeter length and approximately 15 micrometers in diameter [38,39]. During the manufacturing process, carbon fibers tend to align along the compression plane, resulting in anisotropic properties. The direction perpendicular to this plane is referred to as "Through-Thickness" (TT), while the parallel direction is called "In-Plane" (IP). Fig. 2 displays the macro and micro-scale structures of the Calcarb sample examined in this study. Fig. 2(a) presents a macroscopic image of the sample in the IP and TT plane, demonstrating its anisotropy. Fig. 2(b) is a microscopic image captured using a scanning electron microscope (SEM), which

reveals that the diameter of individual carbon fibers is around 15 μm. The porosity of Calcarb, denoted as ε_g, is 0.9.

The microstructure of Calcarb was acquired at the Advanced Light Source at Lawrence Berkeley National Laboratory by Borner et al. [21]. Each scan involved capturing 1024 radiographs over a 180° rotation, utilizing X-ray energy of 14 keV. They used the computed micro-tomography image displayed in Fig. 3 to investigate the flow of rarefied gas in Calcarb. In this work, we used the same image to study inertial effects. The micro-structure is characterized by fibers preferentially aligned at about ±15° with one of the planes (that perpendicular to the direction of compression during manufacturing) [21]. Fig. 4 shows the relationship between cube dimension and porosity, showcasing four 3D models that represent the structures of samples
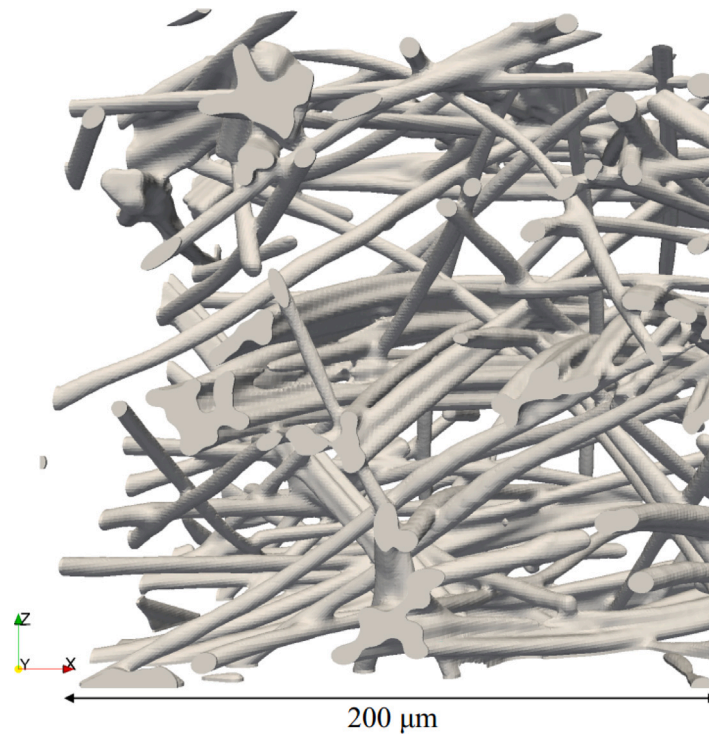
Fig. 3. Volume rendering of the computed micro-tomography of Calcarb.
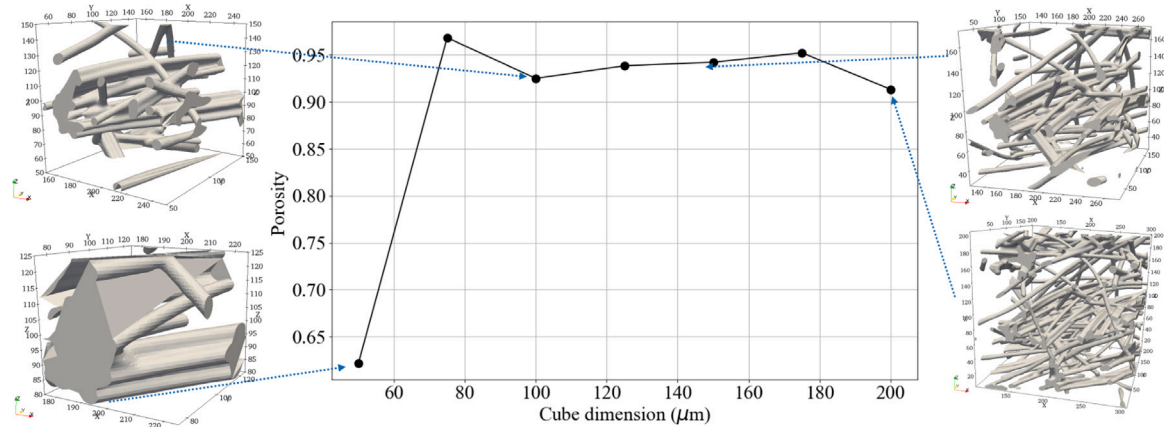
Fig. 4. Relationship between cube dimension and porosity for Calcarb samples.

at dimensions of 50, 100, 150, and 200 μm, respectively. Beyond a cube dimension of 100 μm, the porosity tends to stabilize around 0.93, with fluctuations limited to within 3%. This observation supports the conclusion that the specific geometry studied, namely the 200 μm sample, can be considered representative of the overall structure of Calcarb.

2.3. Data analysis

The one-dimensional flow of compressible fluid through a sample based on Darcy's law is given by the following equation:

$$-\frac{\Delta\langle p\rangle^g}{L} = \frac{\mu}{K} \cdot \frac{q_v}{A} = \frac{\mu^2}{K\rho d_{cl}}Re \tag{3}$$

where $\Delta\langle p\rangle^g$ is the pressure drop measured by the differential pressure transmitter, L is the length of the sample, μ is the gas viscosity at room temperature, q_v is the volumetric flow rate set by the mass flow controller, and A is the cross-section of the sample. Eq. (3) is applicable when the Reynolds number ($Re = \rho(q_v/A)d_{cl}/\mu$) is smaller than 0.5, where d_{cl} is fiber cluster diameter. Due to the manufacturing process, there are clusters of fibers made of five to ten fibers. The mean diameter of the fiber clusters has been shown to be the most relevant characteristic length to compute the Reynolds number [20]. The components of **K** in the IP and TT directions were determined using Eq. (3). For higher Reynolds number, the one-dimensional flow based on the Forchheimer equation is expressed as follows:

Fig. 5. Three-dimensional numerical model used in micro-scale simulation.

$$-\frac{\Delta\langle p\rangle^g}{L} = \frac{\mu}{K}\cdot\frac{q_v}{A} + \rho\beta(\frac{q_v}{A})^n = \frac{\mu^2}{K\rho d_{cl}}Re + \frac{\beta\mu^2}{\rho d_{cl}{}^2}Re^n \qquad (4)$$

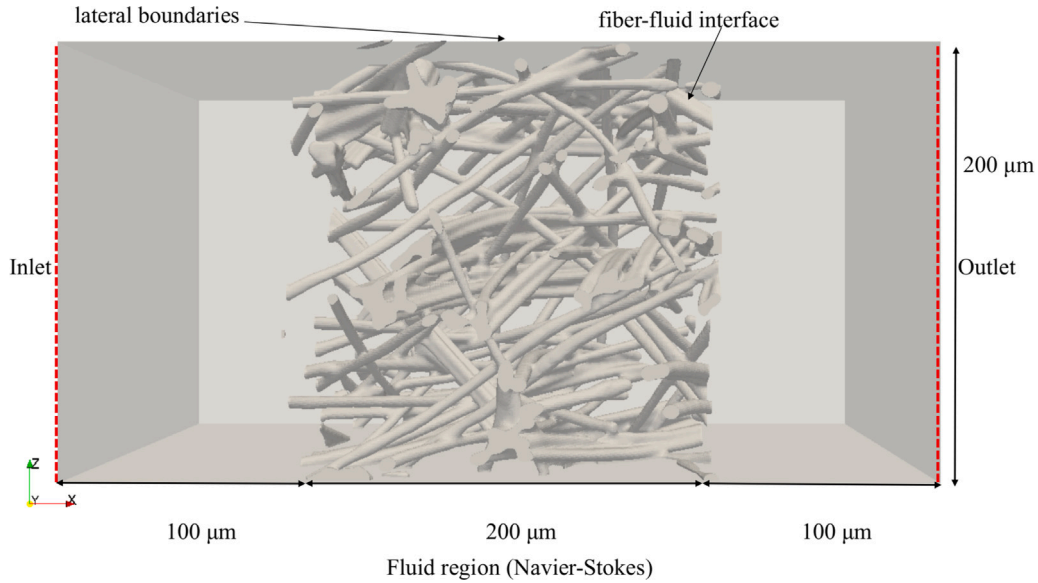where β is the Forchheimer coefficient. The value of the exponent n is typically 2. At a low Reynolds number, the last term disappears, and the Forchheimer equation reduces to Darcy's law. The data analysis method involves initially defining an effective permeability K_{eff}, as specified in Eq. (5). It is crucial to note that within the range of Darcy's Law, the effective permeability remains constant, representing the permeability K we aim to find. Conversely, within the Forchheimer regime, the effective permeability encompasses both the permeability K and a term involving the Forchheimer coefficient β. This allows us to achieve two objectives: first, determine the critical Reynolds number separating the two flow regimes, and second, obtain the permeability K within the Darcy regime by fitting the data to Eq. (3), while acquiring the Forchheimer coefficient β within the Forchheimer regime by fitting the data to Eq. (4).

$$K_{eff} = -\frac{q_v}{A}\cdot\mu\cdot\frac{L}{\Delta\langle p\rangle^g} = -\frac{\mu^2}{\rho d_{cl}}\frac{L}{\Delta\langle p\rangle^g}Re \qquad (5)$$

The values of β and the exponent n can be computed using the least-squares approximation method.

3. Numerical method

In this section, tomographic image-based micro-scale simulations are employed to investigate the incompressible flow of gas within the anisotropic Calcarb sample. The isothermal condition and the variation in pressure in the domain justify the assumption of incompressible flow. The structure of the Calcarb under investigation is obtained through tomography scanning. Classical Navier–Stokes equations are solved at the pore scale, and the pressure drop is investigated under steady-state conditions across the sample. Ultimately, the permeability tensor and the Forchheimer correction tensor are analyzed.

3.1. Numerical model

To determine the permeability and Forchheimer correction tensor, micro-scale simulations must be conducted through a three-dimensional digitized microstructure (Fig. 5). Detailed information regarding the sample can be found in Section 2.2.

Table 2
Boundary conditions for the micro-scale simulation.

Fluid	Inlet	Outlet	Lateral boundaries	Fiber-fluid interface
$\mathbf{v_g}$	*fixed value*	*zero gradient*	*slip*	*noslip*
p	*zero gradient*	*fixed value*	*zero gradient*	*zero gradient*

3.1.1. Mathematical model and numerical implementation

The fluid region is modeled using the transient laminar Navier–Stokes equations (conservation of mass and momentum) at the pore scale, as presented in Eq. (6).

$$\begin{cases} \nabla\cdot\mathbf{v_g} = 0 \\ \rho(\frac{\partial\mathbf{v_g}}{\partial t} + \mathbf{v_g}\cdot\nabla\mathbf{v_g}) = -\nabla p + \mu\nabla^2\mathbf{v_g} \\ \mathbf{v_g} = 0 \quad \text{at} \quad A_{gs} \end{cases} \qquad (6)$$

where $\mathbf{v_g}$ and p are, respectively, the velocity and pressure of the gas phase; A_{gs} represents the interface area between the gas phase and the solid phase contained within the considered region.

Detailed descriptions of the boundary conditions for the system in Eq. (6) are provided in Table 2. These boundary conditions have been demonstrated to be the most suitable for non-periodic porous materials and have been employed in previous studies for permeability calculations [20]. In this work, it is assumed that these boundary conditions are also suitable for the determination of the Forchheimer correction tensor. Regarding velocity, the *slip* condition maintains the tangential velocity at the lateral boundaries while setting the normal component to zero. For pressure, the *zero gradient* condition ensures that the pressure gradient normal to the lateral boundaries is zero. On the fiber-fluid interface, the *noslip* condition is applied to the fluid motion.

The numerical model was implemented in finite volumes in the Porous material Analysis Toolbox based on OpenFOAM (PATO) [15]. Fluid flow was solved with the pimpleFoam solver, which combines the pressure-implicit split-operator (PISO) and semi-implicit method for pressure-linked equations (SIMPLE) algorithms [40]. Second-order schemes, with flux limiters, were used for spatial discretization.
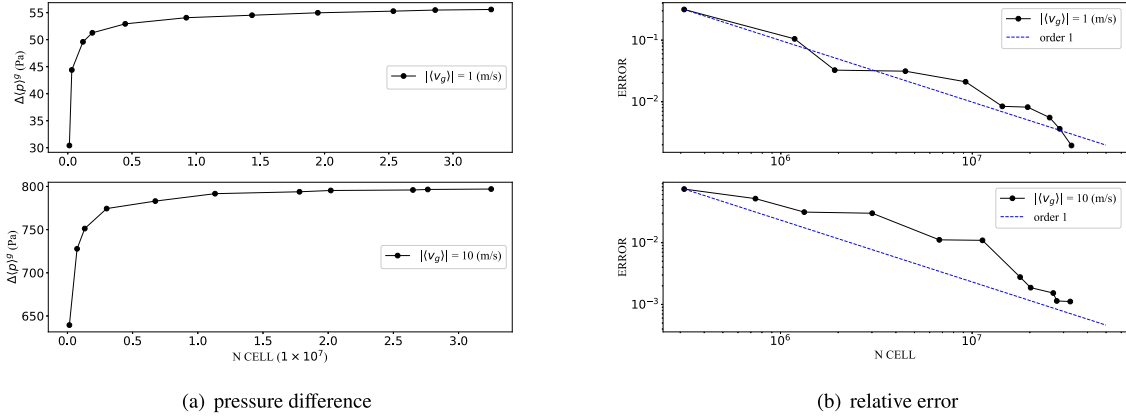
(a) pressure difference

(b) relative error

Fig. 6. Mesh convergence analysis results.

3.1.2. Mesh convergence analysis

The OpenFOAM automatic mesher, *snappyHexMesh*, [41] was utilized to mesh the fluid domain between the fibers. This tool is a mesh manipulation software that allows users to refine a given background mesh into a desired configuration. The meshing algorithm functions through three primary steps. First, a background mesh is created. Then, the carbon fibers' surface is overlaid onto the background mesh. The algorithm identifies cells that are intersected by the carbon fibers' surface and subsequently subdivides them into four parts, generating mesh refinement near the body surface. Following this, the mesh points in close proximity to the body surface are moved to align with the surface, ensuring that the boundary surfaces of the mesh adhere closely to the prescribed geometry. The quality of the final mesh is highly dependent on the settings of various parameters.

Once the parameter configuration process is determined, the next step involves performing a mesh independence verification to ensure that the final mesh does not influence the simulation results. Micro-scale simulations are conducted with varying mesh refinement levels, with changes in specific physical quantities being monitored. In this case, the pressure difference between the inlet and outlet is chosen as an appropriate criterion for evaluating mesh convergence. Two distinct inlet velocities, corresponding to two different Reynolds numbers ($Re = \rho|\langle v_g \rangle| d_{cl}/\mu$), were selected to incorporate the Forchheimer flow regime into the mesh analysis. A mesh convergence study was carried out, ensuring that the pressure residuals remained below 10^{-6} and the velocity residuals below 10^{-8}. Fig. 6 shows the mesh convergence analysis results. Fig. 6(a) presents the convergence of the pressure drop as the mesh is refined. Starting from a small value (e.g., 30 Pa when the inlet velocity is 1 m/s) for a coarse mesh, the pressure drop rapidly converges towards a stabilized value (e.g., 55 Pa). Fig. 6(b) plots the numerical error between two consecutive simulations, which is defined as:

$$ERROR = \frac{\Delta \langle p \rangle_{n+1}^g - \Delta \langle p \rangle_n^g}{\Delta \langle p \rangle_{n+1}^g} \tag{7}$$

where the index n represents the simulation with the mesh before refinement. The blue dotted line corresponds to the first-order slopes. The numerical method is then first order with respect to the discretization. The results suggest that when the number of cells surpasses 20 million, the error gradually decreases until it reaches a steady state

around 1×10^{-2} for $|\langle v_g \rangle| = 1$ m/s and 1×10^{-3} for $|\langle v_g \rangle| = 10$ m/s. Fig. 7 provides some details of the meshed geometry. To meet the computational demands, a portion of the MCIA - (Calculer au Mésocentre regional (curta)) cluster from the University of Bordeaux was utilized, consisting of 6 nodes with 32 cores each (Intel Xeon Gold SKL-6130 @2.1 GHz) and 92 GB of RAM per node. The mesh generation process was completed in 3 h. Additionally, solving the transient laminar Navier–Stokes equations, as referenced in Eq. (6), required 8 h of computational time on the cluster for one case.

3.2. Mathematical description of the Forchheimer term

3.2.1. Description of the Forchheimer correction tensor

For the scales of flow in porous media, upscaling of micro-scale problems has been proposed using either homogenization theory [42] or the volume-averaging technique [43]. The macroscopic model is given by Eq. (8) [14,17,20]. When the Reynolds number is small, the second term $\mathbf{F} \cdot \langle \mathbf{v_g} \rangle$ in Eq. (8) is negligible, validating Darcy's law. In a previous work [20], the case with this term neglected was discussed, and the permeability tensor $\mathbf{K}$ was obtained. In this study, we specifically examine the case where this term is present.

$$\begin{cases} \nabla \cdot \langle \mathbf{v_g} \rangle = 0 \\ \langle \mathbf{v_g} \rangle = -\dfrac{\mathbf{K}}{\mu} \cdot \nabla \langle p \rangle^g - \mathbf{F} \cdot \langle \mathbf{v_g} \rangle \end{cases} \tag{8}$$

The velocity $\mathbf{v_g}$ and pressure p fields at the pore scale are obtained from the resolution of Eq. (6). Then pressure gradients and velocity components are averaged at the macroscopic scale and substituted into Forchheimer's law as shown in Eq. (8). The latter is conveniently expressed as the following system:

$$\begin{cases} \langle v_g \rangle_x = -\dfrac{1}{\mu}\left(K_{xx}\nabla\langle p\rangle_x^g + K_{xy}\nabla\langle p\rangle_y^g + K_{xz}\nabla\langle p\rangle_z^g \right) \\ \qquad -(F_{xx}\langle v_g\rangle_x + F_{xy}\langle v_g\rangle_y + F_{xz}\langle v_g\rangle_z) \\ \langle v_g \rangle_y = -\dfrac{1}{\mu}\left(K_{yx}\nabla\langle p\rangle_x^g + K_{yy}\nabla\langle p\rangle_y^g + K_{yz}\nabla\langle p\rangle_z^g \right) \\ \qquad -(F_{yx}\langle v_g\rangle_x + F_{yy}\langle v_g\rangle_y + F_{yz}\langle v_g\rangle_z) \\ \langle v_g \rangle_z = -\dfrac{1}{\mu}\left(K_{zx}\nabla\langle p\rangle_x^g + K_{zy}\nabla\langle p\rangle_y^g + K_{zz}\nabla\langle p\rangle_z^g \right) \\ \qquad -(F_{zx}\langle v_g\rangle_x + F_{zy}\langle v_g\rangle_y + F_{zz}\langle v_g\rangle_z) \end{cases} \tag{9}$$

Upon completing the micro-scale simulations, the macroscopic velocity components $\langle v_g \rangle_x$, $\langle v_g \rangle_y$, and $\langle v_g \rangle_z$ are determined as average values in the domain. The pressure gradient components throughout the sample, $\nabla\langle p\rangle_x^g$, $\nabla\langle p\rangle_y^g$, and $\nabla\langle p\rangle_z^g$ are determined from the mean pressure values
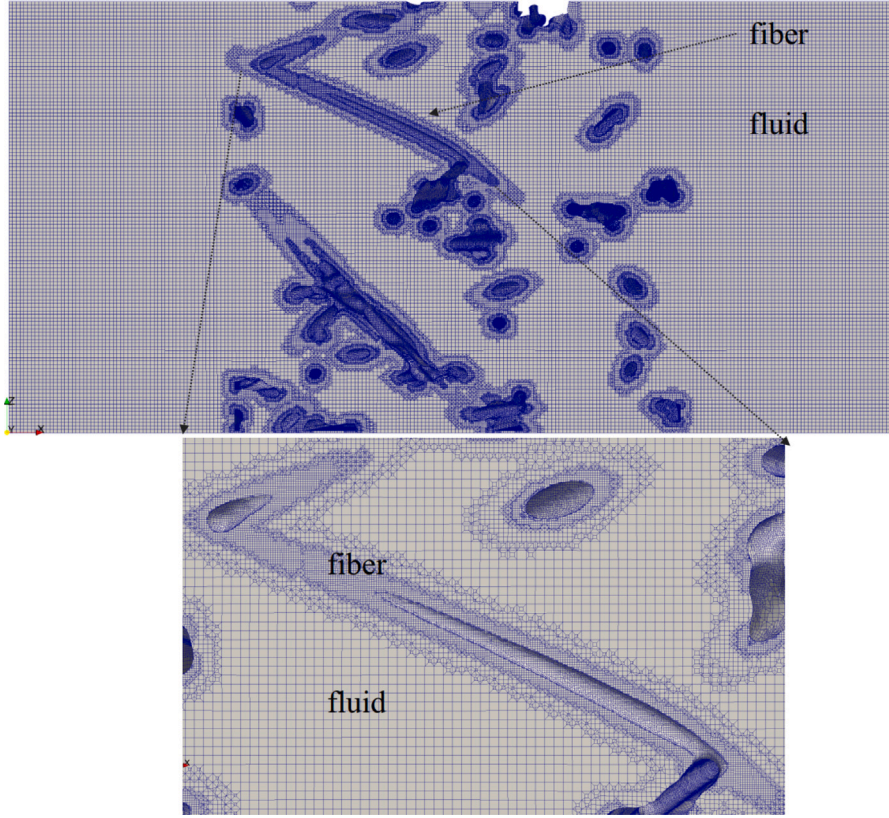
Fig. 7. Details of the meshed geometry.

at the boundaries and the dimensions of the domain in the x, y, and z directions. Since $\mathbf{K}$ is already determined from a simulation at low Re, the remaining unknowns in the system comprise the nine correction tensor components: F_{xx}, F_{xy}, ..., F_{zz}.

Although the tensorial form of the macroscopic inertial resistance has been pointed out clearly [14], the computation of the Forchheimer correction tensor $\mathbf{F}$ (Eq. (8)) is very costly in terms of computation time and resources. Indeed, $\mathbf{F}$ can be computed on a periodic unit cell by solving a tensorial closure problem with a Navier–Stokes structure. The procedure used for the computation of the permeability tensor [20], i.e. imposing a velocity (or pressure gradient) successively along the three directions of the unit cell to obtain the full permeability tensor, is no longer valid here due to the non-linear dependence of $\mathbf{F}$ on $\langle \mathbf{v_g} \rangle$. First of all, for a given direction of the flow, only three components of the $\mathbf{F}$ tensor can be computed. For example, when the inlet velocity is set as (1, 0, 0), indicating the flow direction is along the x-axis, the resulting velocity fields are $\langle v_g \rangle_x = 1.094$ m/s, $\langle v_g \rangle_y = 0.022$ m/s, and $\langle v_g \rangle_z = 0.011$ m/s. Similarly, the corresponding pressure values are $\langle p \rangle_x^g = -50.873$ Pa, $\langle p \rangle_y^g = -4.001$ Pa, and $\langle p \rangle_z^g = -3.122$ Pa. Given that the magnitude of $\langle v_g \rangle_x$ is 49.7 and 99.5 times greater than $\langle v_g \rangle_y$ and $\langle v_g \rangle_z$ respectively, we simplify the problem by neglecting terms related to $\langle v_g \rangle_y$ and $\langle v_g \rangle_z$ in Eq. (8), therefore $F_{xy}\langle v_g \rangle_y$, $F_{xz}\langle v_g \rangle_z$, $F_{yy}\langle v_g \rangle_y$, $F_{yz}\langle v_g \rangle_z$, $F_{zy}\langle v_g \rangle_y$, and $F_{zz}\langle v_g \rangle_z$ are 0. By substituting the known quantities into Eq. (9), we can calculate the values of F_{xx}, F_{yx}, and F_{zx}. In a similar way, when the flow direction is along the y-axis, we can only derive the values of F_{xy}, F_{yy}, and F_{zy}. Lastly, for flow along the z-axis, we can ascertain the values of F_{xz}, F_{yz}, and F_{zz}. Detailed information about $\mathbf{F}$ will be explained in the following Section 4.2.1.

3.2.2. Description of the Forchheimer coefficient tensor

As outlined in Section 1, Wang et al. [23] represented $\mathbf{F}$ as $\mathbf{F} = \rho/\mu|\langle v_g \rangle|(\mathbf{K} \cdot \boldsymbol{\beta})$, assuming $\boldsymbol{\beta}$ to be independent of the gas velocity direction. Thus, $\boldsymbol{\beta}$ is calculated following the same procedure used for the computation of the permeability tensor: applying a velocity successively along the three image directions to derive the full $\boldsymbol{\beta}$ tensor. Tensor $\mathbf{F}$ in Eq. (9) is then transformed into a form involving $\boldsymbol{\beta}$.

$$
\begin{cases}
\langle v_g \rangle_x = -\frac{1}{\mu}\left(K_{xx}\nabla\langle p \rangle_x^g + K_{xy}\nabla\langle p \rangle_y^g + K_{xz}\nabla\langle p \rangle_z^g\right) \\
\quad -\rho/\mu|\langle v_g \rangle|((K_{xx}\beta_{xx} + K_{xy}\beta_{yx} + K_{xz}\beta_{zx})\langle v_g \rangle_x \\
\quad +(K_{xx}\beta_{xy} + K_{xy}\beta_{yy} + K_{xz}\beta_{zy})\langle v_g \rangle_y \\
\quad +(K_{xx}\beta_{xz} + K_{xy}\beta_{yz} + K_{xz}\beta_{zz})\langle v_g \rangle_z) \\
\langle v_g \rangle_y = -\frac{1}{\mu}\left(K_{yx}\nabla\langle p \rangle_x^g + K_{yy}\nabla\langle p \rangle_y^g + K_{yz}\nabla\langle p \rangle_z^g\right) \\
\quad -\rho/\mu|\langle v_g \rangle|((K_{yx}\beta_{xx} + K_{yy}\beta_{yx} + K_{yz}\beta_{zx})\langle v_g \rangle_x \\
\quad +(K_{yx}\beta_{xy} + K_{yy}\beta_{yy} + K_{yz}\beta_{zy})\langle v_g \rangle_y \\
\quad +(K_{yx}\beta_{xz} + K_{yy}\beta_{yz} + K_{yz}\beta_{zz})\langle v_g \rangle_z) \\
\langle v_g \rangle_z = -\frac{1}{\mu}\left(K_{zx}\nabla\langle p \rangle_x^g + K_{zy}\nabla\langle p \rangle_y^g + K_{zz}\nabla\langle p \rangle_z^g\right) \\
\quad -\rho/\mu|\langle v_g \rangle|((K_{zx}\beta_{xx} + K_{zy}\beta_{yx} + K_{zz}\beta_{zx})\langle v_g \rangle_x \\
\quad +(K_{zx}\beta_{xy} + K_{zy}\beta_{yy} + K_{zz}\beta_{zy})\langle v_g \rangle_y \\
\quad +(K_{zx}\beta_{xz} + K_{zy}\beta_{yz} + K_{zz}\beta_{zz})\langle v_g \rangle_z)
\end{cases}
\tag{10}
$$

To establish a closed system, it is essential to perform three simulations, taking into account three distinct flow directions. This method

allows for the creation of a global system of nine equations, as depicted in Eq. (11).

$$
\begin{bmatrix}
\langle v_g \rangle_x^1 \\
\langle v_g \rangle_y^1 \\
\langle v_g \rangle_z^1 \\
\langle v_g \rangle_x^2 \\
\langle v_g \rangle_y^2 \\
\langle v_g \rangle_z^2 \\
\langle v_g \rangle_x^3 \\
\langle v_g \rangle_y^3 \\
\langle v_g \rangle_z^3
\end{bmatrix}
= -\frac{\mathbf{K}\nabla \langle p \rangle^g}{\mu} - \rho/\mu |\langle v_g \rangle|
$$

$$
\times
\begin{bmatrix}
\langle v_g \rangle_x^1 & \langle v_g \rangle_y^1 & \langle v_g \rangle_z^1 & 0 & 0 & 0 & 0 & 0 & 0 \\
0 & 0 & 0 & \langle v_g \rangle_x^1 & \langle v_g \rangle_y^1 & \langle v_g \rangle_z^1 & 0 & 0 & 0 \\
0 & 0 & 0 & 0 & 0 & 0 & \langle v_g \rangle_x^1 & \langle v_g \rangle_y^1 & \langle v_g \rangle_z^1 \\
\langle v_g \rangle_x^2 & \langle v_g \rangle_y^2 & \langle v_g \rangle_z^2 & 0 & 0 & 0 & 0 & 0 & 0 \\
0 & 0 & 0 & \langle v_g \rangle_x^2 & \langle v_g \rangle_y^2 & \langle v_g \rangle_z^2 & 0 & 0 & 0 \\
0 & 0 & 0 & 0 & 0 & 0 & \langle v_g \rangle_x^2 & \langle v_g \rangle_y^2 & \langle v_g \rangle_z^2 \\
\langle v_g \rangle_x^3 & \langle v_g \rangle_y^3 & \langle v_g \rangle_z^3 & 0 & 0 & 0 & 0 & 0 & 0 \\
0 & 0 & 0 & \langle v_g \rangle_x^3 & \langle v_g \rangle_y^3 & \langle v_g \rangle_z^3 & 0 & 0 & 0 \\
0 & 0 & 0 & 0 & 0 & 0 & \langle v_g \rangle_x^3 & \langle v_g \rangle_y^3 & \langle v_g \rangle_z^3
\end{bmatrix}
$$

$$
\times
\begin{bmatrix}
K_{xx}\beta_{xx} + K_{xy}\beta_{yx} + K_{xz}\beta_{zx} \\
K_{xx}\beta_{xy} + K_{xy}\beta_{yy} + K_{xz}\beta_{zy} \\
K_{xx}\beta_{xz} + K_{xy}\beta_{yz} + K_{xz}\beta_{zz} \\
K_{yx}\beta_{xx} + K_{yy}\beta_{yx} + K_{yz}\beta_{zx} \\
K_{yx}\beta_{xy} + K_{yy}\beta_{yy} + K_{yz}\beta_{zy} \\
K_{yx}\beta_{xz} + K_{yy}\beta_{yz} + K_{yz}\beta_{zz} \\
K_{zx}\beta_{xx} + K_{zy}\beta_{yx} + K_{zz}\beta_{zx} \\
K_{zx}\beta_{xy} + K_{zy}\beta_{yy} + K_{zz}\beta_{zy} \\
K_{zx}\beta_{xz} + K_{zy}\beta_{yz} + K_{zz}\beta_{zz}
\end{bmatrix}
\tag{11}
$$

By solving Eq. (11), the product tensor $(\mathbf{K} \cdot \boldsymbol{\beta})$ is obtained. The values of $\boldsymbol{\beta}$ are then computed by applying an inverse operation, i.e., $(\mathbf{K}^{-1} \cdot (\mathbf{K} \cdot \boldsymbol{\beta}))$. Detailed information about $\boldsymbol{\beta}$ will be explained in the following Section 4.2.1.

4. Results and discussions

This section presents a comprehensive analysis of both experimental and simulation results. The experimental results show the pressure drop as a function of gas velocity and utilizing the aforementioned data analysis method, the permeability K and Forchheimer coefficient β are calculated for both IP and TT directions. The simulation results illustrate the relationship between the simulated pressure drop and gas velocity. Based on the simulation methodology, the values of permeability and Forchheimer term are obtained. Furthermore, the gas flow distribution within the sample is discussed in this section. finally, a comparison between the experimental and simulation results is conducted.

4.1. Experimental results

The experimental results are summarized in the Appendix, where q_v represents the gas volume-flow rate, $\langle v_g \rangle$ is the magnitude of the Darcy velocity, and $\Delta \langle p \rangle^g$ denotes the pressure drop between the inlet and outlet. The experimental parameters are as follows: room temperature at 293 K, gas density ρ of 1.17 kg/m^3, gas dynamic viscosity μ of

Table 3
Permeability K in IP and TT direction.

Flow direction	Permeability, K (m^2)	Limit of Re
IP	1.615×10^{-10}	0.43
TT	1.248×10^{-10}	0.31

Table 4
Forchheimer coefficient β (1/m) and exponent n in the IP and TT direction.

Flow direction	β and n ($n = 2$)	β and n ($n \neq 2$)
IP	1.4948×10^5, 2 ($R^2 = 0.9973$)	2.7015×10^5, 1.73 ($R^2 = 0.9999$)
TT	2.0010×10^5, 2 ($R^2 = 0.9993$)	2.7782×10^5, 1.84 ($R^2 = 0.9999$)

1.93×10^{-5} kg/(m s), sample cross-sectional area A of 7.854×10^{-5} m^2, and fiber cluster diameter d_{cl} of 80 μm. Based on the data in Table 6, the experimental results are illustrated in Fig. 8. Fig. 8(a) and (b) display the variations of pressure gradient and effective permeability as a function of the Reynolds number, respectively. The error bars shown in Fig. 8(a) were calculated based on the uncertainties in the experimental process. The effective permeability is calculated using Eq. (5). As demonstrated in Fig. 8(a), the pressure gradient exhibits a non-linear relationship, and the experimental region covers both Darcy and Forchheimer flow regimes. This observation is further supported by Fig. 8(b), where the constant K_{eff} corresponds to the Darcy flow regime. As expected, the obtained permeability in the IP direction is higher than the one in the TT direction.

Fig. 9 provides a detailed view of the Darcy flow region depicted in Fig. 8. The effective permeability is calculated using Eq. (5), representing permeability within the Darcy regime. The obtained permeability values are then used to describe the variation of the pressure gradient shown in Fig. 9(a). The pressure gradient demonstrates a linear relationship in the IP direction when the Reynolds number is less than 0.43 and in the TT direction when the Reynolds number is below 0.31. The permeability, K, values for both IP and TT directions are presented in Table 3.

Within the Forchheimer regime, K values obtained from Table 3 are substituted into Eq. (4), yielding the first coefficient of the polynomial, $\frac{\mu^2}{K\rho d_{cl}}$. Fitting experimental data then enables the ascertainment of the Forchheimer coefficient and the exponent n. This method facilitates describing the intricate relationship between pressure gradient and Reynolds number within the Forchheimer regime. Fig. 10 presents the variation of pressure gradient with respect to Reynolds number in both the IP and TT directions, along with the curves obtained through data fitting. The values of the Forchheimer coefficient β and exponent n are calculated using the least-squares approximation method and presented in Table 4. The classic Forchheimer equation with a fixed exponent of 2 is used to determine the Forchheimer coefficient, as shown in the second column of Table 4, where R^2 represents the model's fit level to the data. The fit is then enhanced by adjusting both the Forchheimer coefficient and the exponent n, with results presented in the third column of the same table. Rather than typically being set as 2, the exponent exhibits minor differences, like Aguilar et al. [24] found in their work with porous rocks. Moreover, the values of β and n are not the same in the IP and TT directions. These disparities arise due to the anisotropy inherent in the sample.

In conclusion, a simple comparison is made between the permeability K, the Forchheimer coefficient β obtained in this study, and the data presented in Table 1. To control for variables, the fit results where the exponent is 2 are selected. The comparison results are displayed in Table 5, where the values of K, taken directly from the experimental results, are specifically $K = 1.615 \times 10^{-10}$ m^2 in the IP direction and 1.248×10^{-10} m^2 in the TT direction, and β was calculated based on the corresponding relationship in Table 1.

The key difference observed is when using the packed bed formula for Calcarb, with results differing by tenfold. In contrast, when using
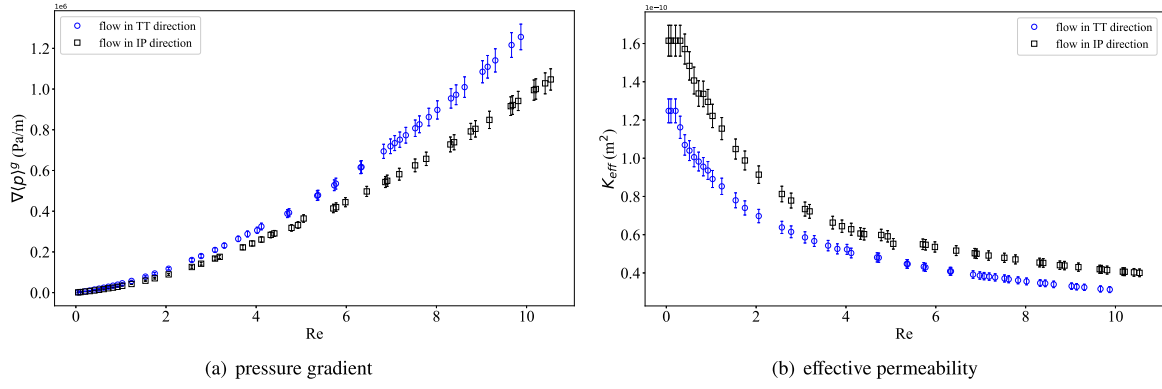
(a) pressure gradient   (b) effective permeability

Fig. 8. Experimental results measured in IP and TT directions.

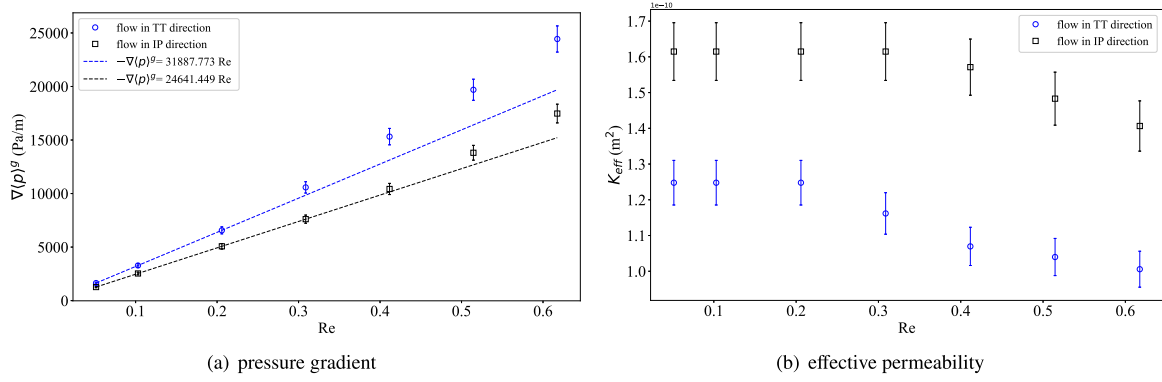(a) pressure gradient   (b) effective permeability

Fig. 9. Pressure gradient and effective permeability in Darcy's regime.
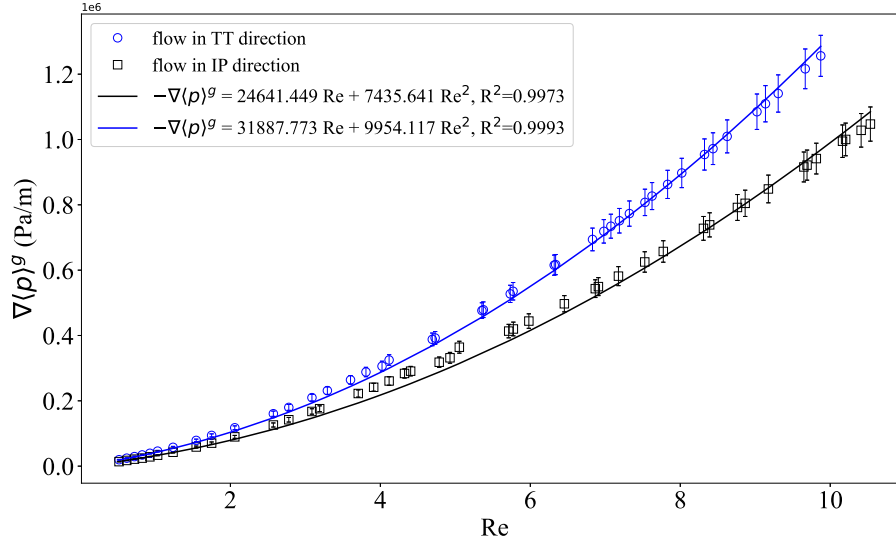
Fig. 10. Relationship between pressure gradient and Reynolds number in both the IP and TT directions.

Table 5
Comparison of the Forchheimer Coefficient β in the IP and TT direction.

Investigators	β (m^{-1})	Remarks
Martin et al. [4]	1.3165×10^4 in IP, 1.4977×10^4 in TT	For packed bed
Petrasch et al. [35]	4.3278×10^4 in IP, 4.9232×10^4 in TT	For porous ceramic
Ahn et al. [37]	9.6157×10^4 in IP, 1.0939×10^5 in TT	For ceramic ablators
Current work	1.4948×10^5 in IP, 2.0010×10^5 in TT	

the formula for ceramic ablators, the closest material to Calcarb, the difference in results is reduced to a twofold difference. However, in the case of ceramic ablators, both calculations remain within the same order of magnitude.

4.2. Numerical results

The relationship between the pressure gradient and flow rate within the Darcy regime was numerically investigated in a previous study by Scandelli et al. [20]. As a crucial material property, the permeability

Fig. 11. Orientation of the original coordinate axes (x, y, z) and principal axes (x', y', z').

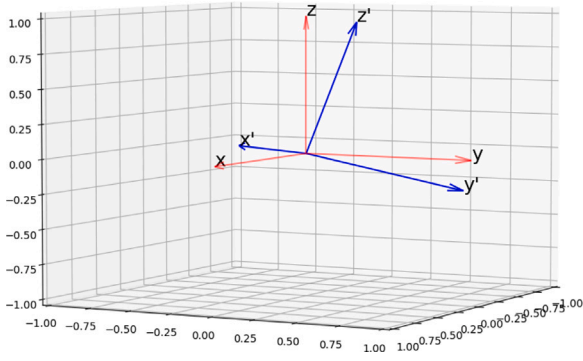tensor of Calcarb, denoted as $\mathbf{K}$, was calculated. For flows in the Darcy regime (Reynolds number less than 0.5), the value of $\mathbf{K}$ was determined accordingly,

$$
\mathbf{K} = \begin{bmatrix} K_{xx} & K_{xy} & K_{xz} \\ K_{yx} & K_{yy} & K_{yz} \\ K_{zx} & K_{zy} & K_{zz} \end{bmatrix}_{x,y,z} m^2
$$
$$
= \begin{bmatrix} 1.561 \times 10^{-10} & 1.391 \times 10^{-11} & 1.021 \times 10^{-11} \\ 1.391 \times 10^{-11} & 1.631 \times 10^{-10} & -5.41 \times 10^{-12} \\ 1.021 \times 10^{-11} & -5.41 \times 10^{-12} & 1.151 \times 10^{-10} \end{bmatrix} m^2
$$
(12)

A diagonalization procedure is employed to rewrite the permeability tensor K in alignment with the principal axes of rotation. The diagonal matrix $\mathbf{K_{dg}}$ is obtained using the relation $\mathbf{K_{dg}} = \mathbf{P}^{-1}\mathbf{KP}$, where $\mathbf{P}$ is change of basis matrix. The values of $\mathbf{K_{dg}}$ and $\mathbf{P}$ are presented in Eq. (13), with x', y', z' oriented relative to IP, IP, and TT. Fig. 11 presents the direction of the original coordinates axes x, y, z and the principal axes x', y', and z' (in blue).

$$
\mathbf{K_{dg}} = \begin{bmatrix} K_{x'x'} & 0 & 0 \\ 0 & K_{y'y'} & 0 \\ 0 & 0 & K_{z'z'} \end{bmatrix}_{x',y',z'} m^2
$$
$$
= \begin{bmatrix} 1.741 \times 10^{-10} & 0 & 0 \\ 0 & 1.491 \times 10^{-10} & 0 \\ 0 & 0 & 1.111 \times 10^{-10} \end{bmatrix} m^2,
$$
(13)
$$
\mathbf{P} = \begin{bmatrix} -0.6258 & -0.7322 & -0.2686 \\ -0.7790 & 0.6031 & 0.1709 \\ -0.0369 & -0.3163 & 0.9479 \end{bmatrix}
$$

In Eq. (13), both $K_{x'x'}$ and $K_{y'y'}$ values correspond to the permeability in the IP direction. However, due to micro-structural factors, these two values are not identical.

In this subsection, a case involving flow within the Forchheimer regime is discussed, highlighting the simulation results and the method used to process the data. The numerical results obtained at various flow velocities are then analyzed to further clarify the behavior of the system.

4.2.1. Velocity fields and Forchheimer correction tensor

In this particular case, an inlet velocity of 1 m/s is chosen, which corresponds to a Reynolds number of 4.85, indicating that the flow lies within the Forchheimer regime. As discussed in Section 3.2, the flow velocities for these simulations are set as (1,0,0), (0,1,0), and (0,0,1). Fig. 12 presents the streamlines within the computational domain, where (a), (b), and (c) respectively correspond to the inlet flow directions along the x, y, and z axes. The streamlines are color-coded based

on the velocity magnitude. Fig. 12 reveals that the maximum gas flow velocity inside the fluid domain can reach values as high as 4.2 m/s, highlighting the complex flow behavior within the porous medium. In each simulation, the pressure gradients $\nabla\langle p\rangle_x^g$, $\nabla\langle p\rangle_y^g$, and $\nabla\langle p\rangle_z^g$ are determined by calculating the average pressure at the interface between the flow and the sample. Simultaneously, the three macroscopic flow velocities, $\langle v_g\rangle_x$, $\langle v_g\rangle_y$, and $\langle v_g\rangle_z$, are obtained by averaging the velocities within the sample. After completing the three simulations, the nine components of the pressure gradients and macroscopic flow velocities can be derived. The next step involves substituting all known values into Eq. (9) to determine the unknown Forchheimer correction tensor $\mathbf{F}$. In this specific case, the computable terms of the Forchheimer correction tensor $\mathbf{F}$ for the inlet velocities of (1,0,0), (0,1,0) and (0,0,1) are respectively computed as follows:

$$
\mathbf{F} = \begin{bmatrix} F_{xx} \\ F_{yx} \\ F_{zx} \end{bmatrix}_{x,y,z} = \begin{bmatrix} 0.901 \\ 0.318 \\ 0.202 \end{bmatrix}, \quad \mathbf{F} = \begin{bmatrix} F_{xy} \\ F_{yy} \\ F_{zy} \end{bmatrix}_{x,y,z} = \begin{bmatrix} 0.308 \\ 0.898 \\ 0.019 \end{bmatrix},
$$
$$
\mathbf{F} = \begin{bmatrix} F_{xz} \\ F_{yz} \\ F_{zz} \end{bmatrix}_{x,y,z} = \begin{bmatrix} 0.413 \\ 0.096 \\ 0.843 \end{bmatrix}
$$
(14)

For each boundary condition, nine components of the tensor $\mathbf{F}$ cannot be obtained. Instead, for a specific flow direction, only three components of the $\mathbf{F}$ tensor can be computed. This restriction results from the non-linear dependency of $\mathbf{F}$ on $\langle \mathbf{v_g}\rangle$. Despite the significant off-diagonal elements, as suggested by the data from Eq. (14), we still provide reference values for β calculated by the formula $\beta_{ii} = \frac{F_{ii}\mu}{K_{ii}\rho|\langle v_g\rangle|}$, where $ii = xx$ or yy or zz. The values in the xx, yy and zz directions are 0.8452×10^5 m^{-1}, 0.9837×10^5 m^{-1}, and 1.2392×10^5 m^{-1}, respectively. These values, although simplistic, are of the same order of magnitude as the experimental values and thus serve as a rough reference. However, it is worth noting that a more comprehensive approach considering the off-diagonal elements would be necessary for a more accurate comparison.

Now, let us adopt the method proposed by Wang et al. [23], as described in Section 3.2.2, to directly compute the Forchheimer coefficient tensor using Eq. (11). The same cases are employed, wherein the inlet gas velocities are respectively set as (1,0,0), (0,1,0), and (0,0,1). The computed value of $\boldsymbol{\beta}$ is found to be.

$$
\boldsymbol{\beta} = \begin{bmatrix} \beta_{xx} & \beta_{xy} & \beta_{xz} \\ \beta_{yx} & \beta_{yy} & \beta_{yz} \\ \beta_{zx} & \beta_{zy} & \beta_{zz} \end{bmatrix}_{x,y,z} m^{-1} = \begin{bmatrix} 0.915 \times 10^5 & 0.243 \times 10^5 & 0.350 \times 10^5 \\ 0.250 \times 10^5 & 0.889 \times 10^5 & 0.107 \times 10^5 \\ 0.221 \times 10^5 & 0.049 \times 10^5 & 1.183 \times 10^5 \end{bmatrix} m^{-1}
$$
(15)

In the experiment, the value of $\boldsymbol{\beta}$ was obtained as $[1.4948 \times 10^5, 0, 0, 0, 1.4948 \times 10^5, 0, 0, 0, 2.0010 \times 10^5]$ m^{-1} (Table 4), while in Eq. (15), the full components of tensor $\boldsymbol{\beta}$ were acquired. To compare results with Eq. (15), a diagonalization procedure is necessary to align the tensor with the principal axes of rotation.

$$
\boldsymbol{\beta_{dg}} = \begin{bmatrix} \beta_{x'x'} & 0 & 0 \\ 0 & \beta_{y'y'} & 0 \\ 0 & 0 & \beta_{z'z'} \end{bmatrix}_{x',y',z'} m^{-1}
$$
$$
= \begin{bmatrix} 1.432 \times 10^5 & 0 & 0 \\ 0 & 0.612 \times 10^5 & 0 \\ 0 & 0 & 0.942 \times 10^5 \end{bmatrix} m^{-1}
$$
(16)

Fig. 13 presents the direction of the original coordinates axes x, y, z and the principal axes x', y', and z' (in blue). It should be noted that the value of $\boldsymbol{\beta_{dg}}$ we obtained is in the principal axes (x', y', z'), whereas the $\boldsymbol{\beta}$ value obtained experimentally is in the original coordinate axes

(a) Flow in the x direction

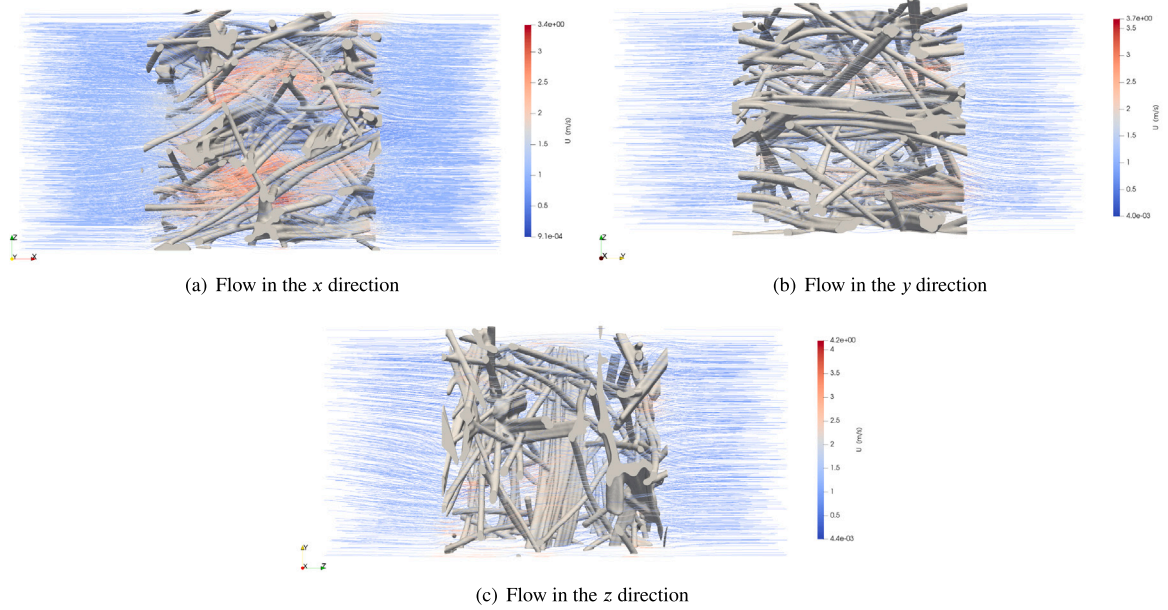(b) Flow in the y direction

(c) Flow in the z direction

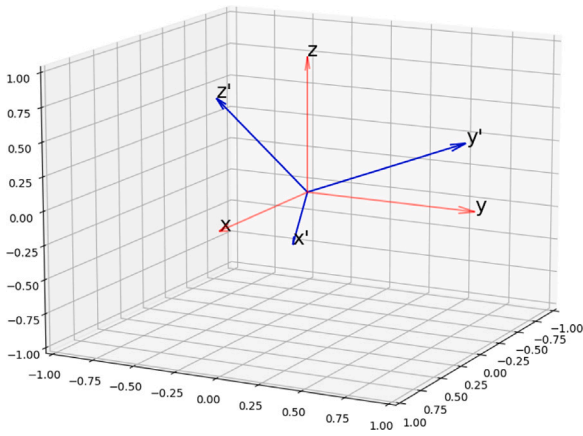Fig. 12. Streamlines visualization in the domain.

Fig. 13. Orientation of the original coordinate axes (x, y, z) and principal axes (x', y', z').

(x, y, z). Although they have the same order, a direct comparison is not feasible.

4.2.2. Analysis of the pressure gradient and Forchheimer term

In order to extend the numerical computation of the pressure gradient to encompass various fluid velocities $\langle v_g \rangle$, the Reynolds number is incorporated into the analysis. Fig. 14 presents the relationship between the pressure gradient components and the Reynolds number for inlet velocities spanning from 0.1 m/s to 10 m/s, corresponding to a Reynolds number range of 0.48 to 48.50, The pressure values obtained from each simulation are depicted using a consistent color scheme. The components $\nabla\langle p\rangle_x^{g1}$, $\nabla\langle p\rangle_y^{g2}$, and $\nabla\langle p\rangle_z^{g3}$ signify the pressure gradient when the inlet flow is aligned with the x, y, and z directions, respectively. The pressure gradient values were acquired from micro-scale simulations for nine values of Re. Within this velocity range, the gas flow exhibits Forchheimer regime behavior. Observations from Fig. 14 highlight several key points. The pressure gradient components $\nabla\langle p\rangle_x^{g1}$, $\nabla\langle p\rangle_y^{g2}$, and $\nabla\langle p\rangle_z^{g3}$ display a nonlinear behavior as the Reynolds number increases, which can be related to the Forchheimer equation as represented by the fitted curves in Eqs. (17) and (18). It should be

noted that the differing methodologies in these equations. Eq. (17) fits only the quadratic coefficient and exponent, keeping the linear term constant, whereas Eq. (18) fits all terms. Additionally, the pressure gradient component $\nabla\langle p\rangle_z^{g3}$ is notably larger than $\nabla\langle p\rangle_x^{g1}$ and $\nabla\langle p\rangle_y^{g2}$ at the same Reynolds number, indicating the anisotropy of the sample. To further explore the relationship between pressure gradient and Reynolds number quantitatively, the concept of the Forchheimer term ($\alpha = \mathbf{F} \cdot \langle v_g \rangle$) is introduced, providing valuable insights into the flow behavior.

$$
\begin{cases}
\nabla\langle p\rangle_x^{g1} = \dfrac{\mu^2}{K_{xx}\rho d_{cl}} Re + \dfrac{\beta\mu^2}{\rho d_{cl}^2} Re^n = 25493.8758\,Re + 9088.99\,Re^{1.47} \\[2mm]
\nabla\langle p\rangle_y^{g2} = \dfrac{\mu^2}{K_{yy}\rho d_{cl}} Re + \dfrac{\beta\mu^2}{\rho d_{cl}^2} Re^n = 24399.7180\,Re + 9643.5539\,Re^{1.43} \\[2mm]
\nabla\langle p\rangle_z^{g3} = \dfrac{\mu^2}{K_{zz}\rho d_{cl}} Re + \dfrac{\beta\mu^2}{\rho d_{cl}^2} Re^n = 34575.1001\,Re + 10849.9677\,Re^{1.49}
\end{cases}
\tag{17}
$$

$$
\begin{cases}
\nabla\langle p\rangle_x^{g1} = 47800.6792\,Re + 740.9160\,Re^{1.98} \\[1mm]
\nabla\langle p\rangle_y^{g2} = 46096.1828\,Re + 772.4158\,Re^{1.94} \\[1mm]
\nabla\langle p\rangle_z^{g3} = 67022.1892\,Re + 418.0495\,Re^{2.15}
\end{cases}
\tag{18}
$$

The Forchheimer term, α, is the product of the Forchheimer correction tensor $\mathbf{F}$ and Darcy velocity $\langle \mathbf{v_g} \rangle$. As can be derived from Eq. (2), this term can also be computed using the following expression:

$$
\alpha = -\langle \mathbf{v_g} \rangle - \frac{\mathbf{K}}{\mu} \cdot \nabla\langle p\rangle^g
\tag{19}
$$

In one-dimensional Forchheimer flow, the Forchheimer term is expected to be proportional to the square of the Darcy velocity. To analyze the impact of anisotropy on this term, the Forchheimer term is calculated using the micro-scale simulation results. Fig. 15(a) illustrates all components of the vector α, exhibiting an increasing tendency. The different colors of the dots in Fig. 15(a) represent the results of simulations with varying Reynolds numbers, with red, blue, and black dots corresponding to the first, second, and third simulations, respectively. The components α_x^1, α_y^2, and α_z^3 denote the Forchheimer term when the inlet flow is aligned with the x, y, and z directions, respectively. Although the values of these three components are higher than the other six, the other components should not be disregarded. For example, the value of α_x^1 is approximately 25% of the value of α_z^3. The value of α_x^1, α_y^2, and α_z^3 is directly proportional to Re^n, where n is not
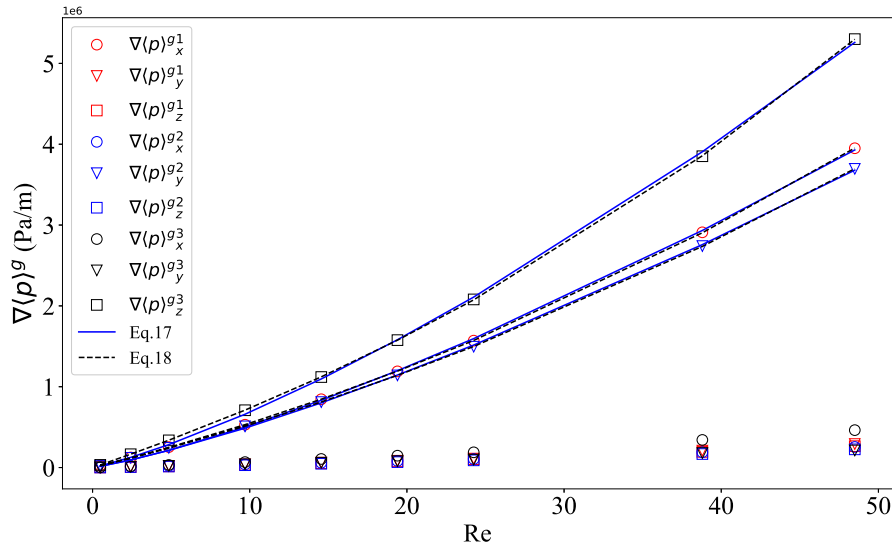
Fig. 14. Pressure gradient components of the digitalized Calcarb domain by varying the *Re*.
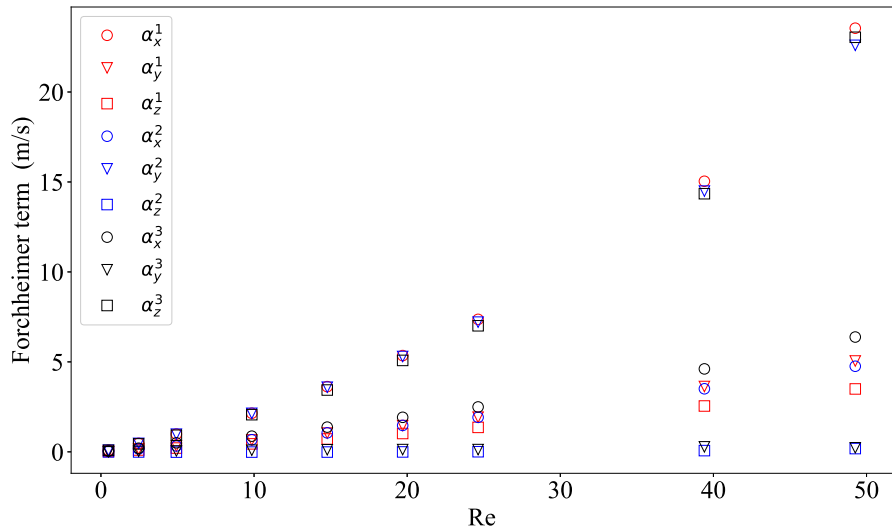

Fig. 15. Forchheimer terms estimated from the numerical solution as a function of Reynolds number. (For interpretation of the references to color in this figure legend, the reader is referred to the web version of this article.)

simply equal to 2 ($n = 1.62$, 1.59 and 1.65 in x, y and z directions), suggesting a more complex relationship between the Forchheimer term and the Reynolds number.

4.3. Comparison with experiment

The strategy for comparing experimental and simulation results focuses on the pressure gradient. In the experiments, the permeability, the Forchheimer coefficient, and the exponent in the IP and TT directions are determined by fitting the experimental data using one-dimensional Darcy and Forchheimer equations. In the simulations, the permeability tensor in the Darcy flow regime is extracted. Then, through a transformation of the principal axes, the diagonal permeability tensor components $K_{dg_{x'x'}}$, $K_{dg_{y'y'}}$ and $K_{dg_{z'z'}}$ are derived, corresponding to the IP, IP and TT directions in the experimental process. In the Forchheimer flow regime, pressure gradients are obtained.

Fig. 16 presents a typical comparison of experimental and simulation results within the Darcy flow regime, where the range of Reynolds number in the experiments ranges from 0.05 to 0.50. In this figure, the

experimental data in the IP and TT directions are represented by solid blue and dashed black lines, respectively, while the simulation results in the x, y, and z directions, labeled as $\nabla\langle p\rangle^{g1}_x$, $\nabla\langle p\rangle^{g2}_y$, and $\nabla\langle p\rangle^{g3}_z$, are represented by circular, triangular, and square markers. It can be observed that the boundary of the Darcy flow regime for Calcarb, based on numerical results, is around 0.24, with a minor difference between the IP and TT directions. Both simulation and experimental results demonstrate that pressure increases linearly with the Reynolds number when it is below 0.24. Fig. 16(b) shows the permeability K remains constant in the Darcy flow regime. The experimental results indicate that the values of K are 1.615×10^{-10} m² and 1.248×10^{-10} m² in the IP and TT directions, respectively. In the simulations, the corresponding values in the x' or y' (IP) and z' (TT) directions are 1.741×10^{-10} or 1.491×10^{-10} m² and 1.111×10^{-10} m². The results exhibit a relative difference of around 8% within the Darcy flow regime.

Fig. 17 presents the comparison of experimental and simulation results within the Forchheimer flow regime, where the Reynolds number in the experiments ranges from 0.50 to 9.8. In this figure, the same symbols mentioned earlier are used to represent the respective data
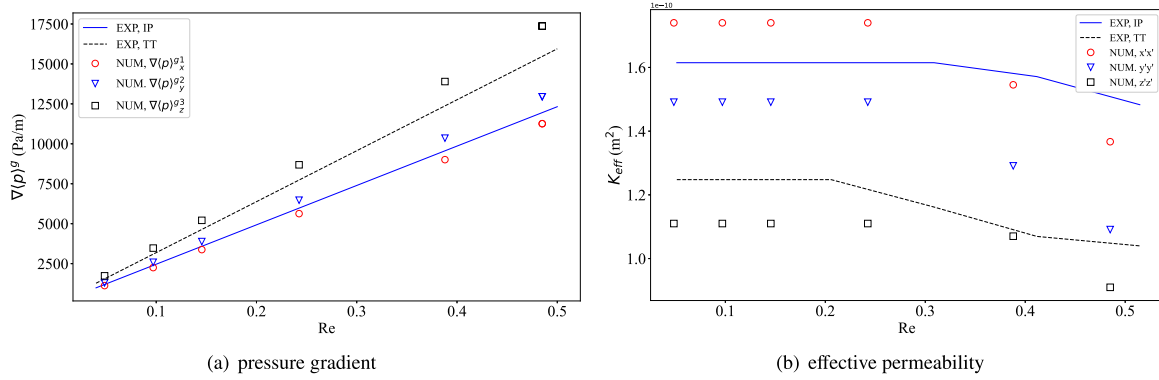
(a) pressure gradient

(b) effective permeability

Fig. 16. The comparison between numerical and experimental results in the Darcy flow regime.
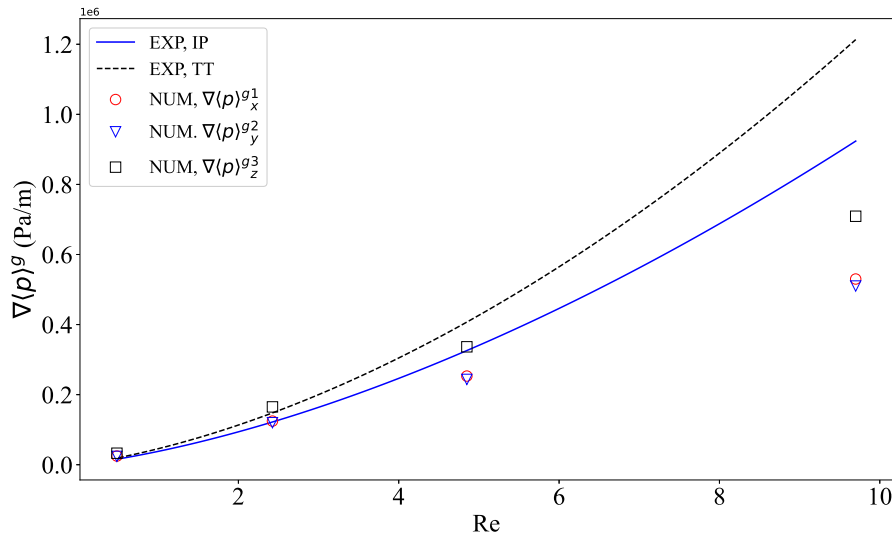

Fig. 17. The comparison of numerical and experiment results in the Forchheimer flow regime.

points. The data representing the experimental correlations are sourced from Table 4 ($n = 2$). When comparing values within the Forchheimer flow regime, one can notice that the maximal differences in pressure gradient between simulation and experiment reach up to 64.5% and 68.2% in the IP and TT directions respectively. Given the assumption of one-dimensional flow in the experiments, only the pressure drop in the direction of flow was taken into account. However, in the three-dimensional simulation, the dispersion of flow due to pressure drop in other directions was also considered. This dispersion, occurring in directions other than the main flow, leads to a decrease in pressure drop along the main flow direction, which could result in simulation values being lower than experimental values. Furthermore, as displayed in Fig. 17, when the Reynolds number is less than 2.4, the difference between the simulation and experimental values is 4.5% and 5.2% in the IP and TT directions, respectively. As the Reynolds number increases, the pressure gradient components in non-main flow directions become more significant, causing the simulated pressure drop along the main flow direction to diverge increasingly from the experimental value.

5. Conclusion

The objective of this work was to identify the validity domain of Darcy or Darcy-Forchheimer flow regime in terms of a critical Reynolds (Re_c) and to determine macroscopic properties, namely, the permeability and Forchheimer tensors by performing experimental and

X-ray tomographic image-based characterization of Calcarb. For this purpose, an experimental facility was designed to measure the pressure gradient across Calcarb samples in these two regimes. Experiments were conducted using nitrogen as the working fluid, for Reynolds numbers ranging from 0.05 to 10.46, and in both in-plane (IP) and through-thickness (TT) orientations. Based on the experimental results, the permeability K, the Forchheimer coefficient β were calculated by fitting the experimental data using one-dimensional Darcy or Forchheimer equations. Concurrently, permeability and pressure gradients were computed from micro-scale numerical solutions, using 3D digital images of Calcarb samples. The numerical model was implemented with finite volumes in PATO. Following permeability calculations, the Forchheimer correction tensor **F** was computed and analyzed in terms of fluid velocity.

Experimental results exhibit the anisotropic nature of Calcarb, namely through Re_c values, corresponding to the Darcy flow regime limit, slightly different in the two directions (Re_c of 0.31 and 0.43) with measured permeability values of 1.248×10^{-10} m^2 and 1.615×10^{-10} m^2 for TT and IP directions respectively. In the simulations, the corresponding values in the principal axes z' (TT), and x' or y' (IP) directions, are 1.111×10^{-10} m^2 and 1.741×10^{-10} or 1.491×10^{-10} m^2. The results exhibit a relative difference of around 8% within the Darcy flow regime.

In the Forchheimer regime, experimental Forchheimer coefficients β were 2.0010×10^5 m^{-1} (TT) and 1.4948×10^5 m^{-1} (IP). In the simulation

Table 6
Results of measurements in IP and TT directions.

IP				TT			
q_v ($\times 10^{-5}$, m^3/s)	$\langle v_g \rangle$ ($\frac{q_g}{A}$, m/s)	$\Delta \langle p \rangle^g$ (Pa)	Re ($\frac{\rho \langle v_g \rangle d_{cl}}{\mu}$)	q_v ($\times 10^{-5}$, m^3/s)	$\langle v_g \rangle$ ($\frac{q_g}{A}$, m/s)	$\Delta \langle p \rangle^g$ (Pa)	Re ($\frac{\rho \langle v_g \rangle d_{cl}}{\mu}$)
0.083	0.011	25.36	0.053	0.083	0.011	32.82	0.053
0.167	0.021	50.73	0.106	0.167	0.021	65.65	0.106
0.333	0.042	101.45	0.214	0.333	0.042	131.29	0.214
0.500	0.064	152.18	0.309	0.500	0.064	211.53	0.309
0.667	0.085	208.55	0.409	0.667	0.085	306.35	0.409
0.833	0.106	276.18	0.513	0.833	0.106	393.88	0.513
1.000	0.127	349.45	0.615	1.000	0.127	488.71	0.615
1.167	0.149	428.36	0.719	1.167	0.149	583.53	0.719
1.333	0.170	490.36	0.822	1.333	0.170	685.65	0.822
1.500	0.191	569.27	0.925	1.500	0.191	787.76	0.925
1.667	0.212	670.73	1.028	1.667	0.212	919.06	1.028
2.000	0.255	851.09	1.233	2.000	0.255	1152.47	1.233
2.500	0.318	1172.36	1.541	2.500	0.318	1575.53	1.541
2.833	0.361	1409.09	1.744	2.833	0.361	1881.88	1.744
3.333	0.424	1792.36	2.051	3.333	0.424	2348.71	2.051
4.167	0.531	2519.45	2.565	4.167	0.531	3209.41	2.565
4.500	0.573	2840.73	2.770	4.500	0.573	3596.00	2.770
5.000	0.637	3348.00	3.077	5.000	0.637	4194.12	3.077
5.167	0.658	3517.09	3.176	5.333	0.679	4624.47	3.261
6.000	0.764	4447.09	3.694	5.833	0.743	5280.94	3.590
6.333	0.806	4830.36	3.893	6.167	0.785	5762.35	3.787
6.667	0.849	5213.64	4.102	6.514	0.829	6119.76	4.003
7.000	0.891	5675.82	4.309	6.667	0.849	6499.06	4.102
7.132	0.908	5816.73	4.392	7.599	0.968	7760.94	4.676
7.748	0.987	6363.45	4.758	7.661	0.975	7848.47	4.804
7.982	1.016	6634.00	4.915	8.671	1.104	9526.12	5.327
8.183	1.042	7282.18	5.023	8.702	1.108	9577.18	5.353
9.250	1.178	8268.55	5.681	9.283	1.182	10547.29	5.715
9.350	1.191	8398.18	5.757	9.344	1.190	10707.76	5.723
9.685	1.233	8882.91	5.946	10.263	1.307	12341.65	6.306
10.452	1.331	9942.55	6.421	10.232	1.303	12305.18	6.281
11.120	1.416	10866.91	6.832	11.060	1.408	13880.71	6.780
11.187	1.424	10990.91	6.870	11.304	1.439	14376.71	6.994
11.620	1.480	11633.45	7.133	11.457	1.459	14690.35	7.130
12.188	1.552	12501.45	7.485	11.641	1.482	15025.88	7.161
12.588	1.603	13144.00	7.728	11.856	1.510	15463.53	7.301
13.457	1.713	14558.73	8.259	12.193	1.552	16149.18	7.509
13.590	1.730	14772.91	8.342	12.346	1.572	16535.76	7.602
14.190	1.807	15838.18	8.708	12.682	1.615	17250.59	7.921
14.357	1.828	16091.82	8.813	12.988	1.654	17950.82	8.133
14.858	1.892	16971.09	9.123	13.479	1.716	19081.41	8.276
15.625	1.989	18318.18	9.597	13.662	1.740	19438.82	8.417
15.693	1.998	18430.91	9.641	13.968	1.779	20190.12	8.597
15.893	2.024	18831.09	9.759	14.612	1.860	21700.00	8.960
16.460	2.096	19896.36	10.110	14.795	1.884	22188.71	9.084
16.527	2.104	20003.45	10.149	15.070	1.919	22816.00	9.290
16.862	2.147	20561.45	10.355	15.654	1.993	24325.88	9.643
17.062	2.172	20944.73	10.464	15.989	2.036	25120.94	9.745

process, the values of all the components of the Forchheimer correction tensor **F** were not yielded. This is attributed to the fact that the computation method for the permeability tensor **K**, which involves successively imposing a velocity (or pressure gradient) along the three unit cell directions, becomes inapplicable due to the non-linear dependence of **F** on $\langle \mathbf{v_g} \rangle$. Instead, we investigated the relationship between pressure gradient $\nabla \langle p \rangle^g$ and Reynolds numbers Re. $\nabla \langle p \rangle^g$ was presented as a function of Re in the three main directions: x, y, and z. The maximal differences in pressure gradient between simulation and experiment reach up to 64.5% and 68.2% in the IP and TT directions, respectively. This difference could be attributed to several factors. which are: (1) The boundary conditions used to solve permeability may require adjustment due to the influence of inertial flow. (2) The chosen 3D images may not be sufficient to ensure the domain's representativeness. (3) The pressure values obtained in the simulation are oriented along the original x, y, and z axes, which differ from the principal axes. These aspects will be examined in our ongoing work.

Declaration of competing interest

The authors declare that they have no known competing financial interests or personal relationships that could have appeared to influence the work reported in this paper.

Acknowledgments

Appendix. Results of measurements in IP and TT directions

See Table 6

References

[1] F. Panerai, J.C. Ferguson, J. Lachaud, A. Martin, M.J. Gasch, N.N. Mansour, Micro-tomography based analysis of thermal conductivity, diffusivity and oxidation behavior of rigid and flexible fibrous insulators, Int. J. Heat Mass Transf. 108 (2017) 801–811, http://dx.doi.org/10.1016/j.ijheatmasstransfer.2016.12.048.

[2] J. Lachaud, I. Cozmuta, N.N. Mansour, Multiscale approach to ablation modeling of phenolic impregnated carbon ablators, J. Spacecr. Rockets 47 (6) (2010) 910–921, http://dx.doi.org/10.2514/1.42681.

[3] R.A. Beck, D.M. Driver, M.J. Wright, H.H. Hwang, K.T. Edquist, S.A. Sepka, Development of the mars science laboratory heatshield thermal protection system, J. Spacecr. Rockets 51 (4) (2014) 1139–1150, http://dx.doi.org/10.2514/1.A32635.

[4] A. Martin, I.D. Boyd, Non-darcian behavior of pyrolysis gas in a thermal protection system, J. Thermophys. Heat Transfer 24 (1) (2010) 60–68, http://dx.doi.org/10.2514/1.44103.

[5] J.R. Gaier, The Effects of Lunar Dust on EVA Systems During the Apollo Missions, Tech. Rep., 2007.

[6] M. Stackpoole, S. Sepka, I. Cozmuta, D. Kontinos, Post-flight evaluation of stardust sample return capsule forebody heatshield material, in: 46th AIAA Aerospace Sciences Meeting and Exhibit, 2008, http://dx.doi.org/10.2514/6.2008-1202.

[7] K.T. Edquist, B.R. Hollis, C.O. Johnston, D. Bose, T.R. White, M. Mahzari, Mars science laboratory heat shield aerothermodynamics: Design and reconstruction, J. Spacecr. Rockets 51 (4) (2014) 1106–1124, http://dx.doi.org/10.2514/1.A32749.

[8] J.B. Meurisse, J. Lachaud, F. Panerai, C. Tang, N.N. Mansour, Multidimensional material response simulations of a full-scale tiled ablative heatshield, Aerosp. Sci. and Technol. 76 (2018) 497–511, http://dx.doi.org/10.1016/j.ast.2018.01.013.

[9] M. Mahzari, R. Beck, H. Hwang, J. Monk, J. Morgan, J. Williams, K.T. Edquist, Development and sizing of the mars2020 thermal protection system, in: AIAA AVIATION 2022 Forum, 2022, p. 3951, http://dx.doi.org/10.2514/6.2022-3951.

[10] E. Pate-Cornell, R. Dillon, Probabilistic risk analysis for the NASA space shuttle: A brief history and current work, Reliab. Eng. Syst. Saf. 74 (3) (2001) 345–352, http://dx.doi.org/10.1016/S0951-8320(01)00081-3.

[11] J. Lachaud, T.E. Magin, I. Cozmuta, N.N. Mansour, A short review of ablative-material response models and simulation tools, in: 7th Aerothermodynamics Symposium, (no. ARC-E-DAA-TN3517) 2011.

[12] A. Martin, I. Boyd, Simulation of pyrolysis gas within a thermal protection system, in: 40th Thermophysics Conference, 2008, p. 3805, http://dx.doi.org/10.2514/6.2008-3805.

[13] F. Panerai, J.D. White, T.J. Cochell, O.M. Schroeder, N.N. Mansour, M.J. Wright, A. Martin, Experimental measurements of the permeability of fibrous carbon at high-temperature, Int. J. Heat Mass Transf. 101 (2016) 267–273, http://dx.doi.org/10.1016/j.ijheatmasstransfer.2016.05.016.

[14] D. Lasseux, A.A. Abbasian Arani, A. Ahmadi, On the stationary macroscopic inertial effects for one phase flow in ordered and disordered porous media, Phys. Fluids 23 (7) (2011) 073103, http://dx.doi.org/10.1063/1.3615514.

[15] J. Lachaud, N.N. Mansour, Porous-material analysis toolbox based on openfoam and applications, J. Thermophys. Heat Transfer 28 (2) (2014) 191–202, http://dx.doi.org/10.2514/1.T4262.

[16] P. Kumar, F. Topin, Investigation of fluid flow properties in open cell foams: Darcy and weak inertia regimes, Chem. Eng. Sci. 116 (2014) 793–805, http://dx.doi.org/10.1016/j.ces.2014.06.009.

[17] S. Whitaker, The Forchheimer equation: A theoretical development, Transp. Porous Media 25 (1) (1996) 27–61, http://dx.doi.org/10.1007/BF00141261.

[18] H. Scandelli, A. Ahmadi-Senichault, J. Lachaud, Two-temperature ablative material response model with application to stardust and MSL atmospheric entries, Aerosp. Sci. Technol. 137 (2023) 108297, http://dx.doi.org/10.1016/j.ast.2023.108297.

[19] S. Liu, A. Ahmadi-Senichault, C. Levet, J. Lachaud, Experimental investigation on the validity of the local thermal equilibrium assumption in ablative-material response models, Aerosp. Sci. Technol. 141 (2023) 108516, http://dx.doi.org/10.1016/j.ast.2023.108516.

[20] H. Scandelli, A. Ahmadi-Senichault, C. Levet, J. Lachaud, Computation of the permeability tensor of non-periodic anisotropic porous media from 3D images, Transp. Porous Media 142 (3) (2022) 669–697, http://dx.doi.org/10.1007/s11242-022-01766-8.

[21] A. Borner, F. Panerai, N. N.Mansour, High temperature permeability of fibrous materials using direct simulation Monte Carlo, Int. J. Heat Mass Transf. 106 (2017) 1318–1326, http://dx.doi.org/10.1016/j.ijheatmasstransfer.2016.10.113.

[22] P. Poureslami, M. Siavashi, H. Moghimi, M. Hosseini, Pore-scale convection-conduction heat transfer and fluid flow in open-cell metal foams: A three-dimensional multiple-relaxation time lattice Boltzmann (MRT-LBM) solution, Int. Commun. Heat Mass Transfer 126 (2021) 105465, http://dx.doi.org/10.1016/j.icheatmasstransfer.2021.105465.

[23] X. Wang, F. Thauvin, K. Mohanty, Non-Darcy flow through anisotropic porous media, Chem. Eng. Sci. 54 (12) (1999) 1859–1869, http://dx.doi.org/10.1016/S0009-2509(99)00018-4.

[24] C. Aguilar-Madera, J. Flores-Cano, V. Matías-Pérez, J. Briones-Carrillo, F. Velasco-Tapia, Computing the permeability and Forchheimer tensor of porous rocks via closure problems and digital images, Adv. Water Resour. 142 (2020) 103616, http://dx.doi.org/10.1016/j.advwatres.2020.103616.

[25] M. Hangi, V. Wheeler, W. Lipiński, Numerical determination of permeability and Forchheimer coefficient in dual-scale porous media, Int. Commun. Heat Mass Transfer 122 (2021) 105089, http://dx.doi.org/10.1016/j.icheatmasstransfer.2020.105089.

[26] A.G. Straatman, N.C. Gallego, Q. Yu, B.E. Thompson, Characterization of porous carbon foam as a material for compact recuperators, J. Eng. Gas Turb. Power 129 (2) (2006) 326–330, http://dx.doi.org/10.1115/1.2436562.

[27] M.D. Innocentini, V.R. Salvini, A. Macedo, V.C. Pandolfelli, Prediction of ceramic foams permeability using Ergun's equation, Mater. Res. 2 (1999) 283–289.

[28] Z. Zeng, R. Grigg, A criterion for non-Darcy flow in porous media, Transp. Porous Media 63 (2006) 57–69, http://dx.doi.org/10.1007/s11242-005-2720-3.

[29] J.T. Gostick, M.W. Fowler, M.D. Pritzker, M.A. Ioannidis, L.M. Behra, In-plane and through-plane gas permeability of carbon fiber electrode backing layers, J. Power Sources 162 (1) (2006) 228–238, http://dx.doi.org/10.1016/j.jpowsour.2006.06.096.

[30] W. Sobieski, A. Trykozko, Darcy's and Forchheimer's Laws in Practice. part 1. The Experiment, Technical Sciences/University of Warmia and Mazury in Olsztyn, 2014.

[31] J. Marschall, F.S. Milos, Gas permeability of rigid fibrous refractory insulations, J. Thermophys. Heat Transfer 12 (4) (1998) 528–535, http://dx.doi.org/10.2514/2.6372.

[32] J. Marschall, M.E. Cox, Gas permeability of lightweight ceramic ablators, J. Thermophys. Heat Transfer 13 (3) (1999) 382–384, http://dx.doi.org/10.2514/2.6451.

[33] S. Ergun, Fluid flow through packed columns, Chem. Eng. Prog. 48 (2) (1952) 89–94.

[34] S. Liu, A. Ahmadi-Senichault, C. Levet, J. Lachaud, Development and validation of a local thermal non-equilibrium model for high-temperature thermal energy storage in packed beds, J. Energy Storage 78 (2024) 109957, http://dx.doi.org/10.1016/j.est.2023.109957.

[35] J. Petrasch, F. Meier, H. Friess, A. Steinfeld, Tomography based determination of permeability, Dupuit–Forchheimer coefficient, and interfacial heat transfer coefficient in reticulate porous ceramics, Int. J. Heat Fluid Flow 29 (1) (2008) 315–326, http://dx.doi.org/10.1016/j.ijheatfluidflow.2007.09.001.

[36] Y.-K. Chen, F.S. Milos, Effects of nonequilibrium chemistry and Darcy—Forchheimer pyrolysis flow for charring ablator, J. Spacecr. Rockets 50 (2) (2013) 256–269, http://dx.doi.org/10.2514/1.A32289.

[37] H.-K. Ahn, C. Park, K. Sawada, Response of heatshield material at stagnation point of Pioneer-Venus probes, J. Thermophys. Heat Transfer 16 (3) (2002) 432–439, http://dx.doi.org/10.2514/2.6697.

[38] H.K. Tran, C.E. Johnson, D.J. Rasky, F.C.L. Hui, M.-T. Hsu, T. Chen, Y.K. Chen, D. Paragas, L. Kobayashi, Phenolic Impregnated Carbon Ablators (PICA) as thermal protection systems for discovery missions, NASA Technical Memorandum 110440 (1997) 1–70, http://dx.doi.org/10.2514/6.1996-1911.

[39] K. Triantou, K. Mergia, S. Florez, B. Perez, J. Bárcena, W. Rotärmel, G. Pinaud, W. Fischer, Thermo-mechanical performance of an ablative/ceramic composite hybrid thermal protection structure for re-entry applications, Compos B 82 (2015) 159–165, http://dx.doi.org/10.1016/j.compositesb.2015.07.020.

[40] H.G. Weller, G. Tabor, H. Jasak, C. Fureby, A tensorial approach to computational continuum mechanics using object-oriented techniques, Comput. Phys. 12 (6) (1998) 620–631, http://dx.doi.org/10.1063/1.168744.

[41] H. Jasak, A. Jemcov, Z. Tukovic, et al., OpenFOAM: A C++ library for complex physics simulations, in: International Workshop on Coupled Methods in Numerical Dynamics, vol. 1000, IUC Dubrovnik Croatia, 2007, pp. 1–20.

[42] C. Mei, J.-L. Auriault, The effect of weak inertia on flow through a porous medium, J. Fluid Mech. 222 (1991) 647–663, http://dx.doi.org/10.1017/S0022112091001258.

[43] S. Whitaker, The Method of Volume Averaging, vol. 13, Springer Science & Business Media, 2013.